Chapter 2

Photon Statistics, Measurements, and Measurements Tools

Martin J. Stevens
National Institute of Standards and Technology, 325 Broadway, Boulder, CO 80305, USA

Chapter Outline

Single-Photon Generation and Detection, Volume 45. http://dx.doi.org/10.1016/B978-0-12-387695-9.00002-0

2.1 QUANTIZED ELECTRIC FIELD & OPERATOR NOTATION

This section introduces some of the basic quantum optics notation found in many textbooks, most closely following the treatments of Gerry and Knight [16], Loudon [25], and Walls and Milburn [47]. Sections 2.2 and 2.3 then detail the characteristics of single-photon sources, and detectors, respectively.

The quantized electric field at position $\vec{\mathbf{r}}$ and time t can be written as an operator,

$$\hat{\mathbf{E}}(\vec{\mathbf{r}},t) = \sum_j \left[\hat{\mathbf{E}}_j^{(+)}(\vec{\mathbf{r}},t) + \hat{\mathbf{E}}_j^{(-)}(\vec{\mathbf{r}},t)\right], \tag{2.1}$$

where the sum is over j orthogonal modes. Each mode j can be defined as having some particular spatial extent, propagation vector, center wavelength, polarization, and spectral and temporal profiles. $\hat{\mathbf{E}}_j^{(+)}(\vec{\mathbf{r}},t)$ and $\hat{\mathbf{E}}_j^{(-)}(\vec{\mathbf{r}},t)$ represent the positive and negative frequency components, respectively, of the field in mode j. They are related as

$$\hat{\mathbf{E}}_j^{(-)}(\vec{\mathbf{r}},t) = \left[\hat{\mathbf{E}}_j^{(+)}(\vec{\mathbf{r}},t)\right]^\dagger, \tag{2.2}$$

where † denotes the Hermitian conjugate.

The electromagnetic field is treated as a quantized harmonic oscillator with a Hamiltonian

$$\hat{H} = \sum_j \hbar\omega_j \left(\hat{a}_j^\dagger \hat{a}_j + \frac{1}{2}\right), \tag{2.3}$$

where $\hbar = h/2\pi$ and h is the Planck constant and $\frac{1}{2}\hbar\omega_j$ is the energy of the vacuum fluctuations in mode j. The single-mode creation operator $\hat{a}_j^\dagger$ denotes the addition of one photon to mode j:

$$\hat{a}_j^\dagger |n\rangle_j = \sqrt{n+1}|n+1\rangle_j, \tag{2.4}$$

where the photon number state $|n\rangle_j$ indicates that exactly n photons occupy mode j. Similarly, the annihilation operator $\hat{a}_j$ describes the removal of one photon from the mode:

$$\hat{a}_j |n\rangle_j = \sqrt{n}|n-1\rangle_j, \tag{2.5}$$

The number states are eigenstates of the single-mode number operator, $\hat{n}_j$, such that

$$\hat{n}_j |n\rangle_j = \hat{a}_j^\dagger \hat{a}_j |n\rangle_j = n|n\rangle_j, \tag{2.6}$$

In perhaps the most commonly cited example of a single-mode field, the mode j can be taken to indicate a plane-wave, monochromatic field with angular

frequency ω_j, wave vector $\vec{\mathbf{k}}_j$, and polarization described by the unit vector $\vec{\mathbf{e}}_j$. The positive-frequency component of the field in this mode can be written as [16]

$$\hat{\mathbf{E}}_j^{(+)}(\vec{\mathbf{r}},t) = \mathcal{E}_j \vec{\mathbf{e}}_j \hat{a}_j e^{i(\vec{\mathbf{k}}_j \cdot \vec{\mathbf{r}} - \omega_j t)}, \tag{2.7}$$

with $\mathcal{E}_j = i\sqrt{\hbar\omega_j/2\varepsilon_0 V}$, where ε_0 is the vacuum permittivity and V is the mode volume.

To describe fields that are not strictly monochromatic, and thus have some non-zero spectral width, it is convenient to replace the single-mode creation and annihilation operators $\hat{a}_j^\dagger$ and $\hat{a}_j$ with their continuous-mode counterparts $\hat{a}_j^\dagger(\omega)$ and $\hat{a}_j(\omega)$. These operators obey the commutation relation [25]

$$[\hat{a}_j(\omega), \hat{a}_j^\dagger(\omega')] = \delta(\omega - \omega'). \tag{2.8}$$

The number operator in this case is rewritten as

$$\hat{n}_j = \int \mathrm{d}\omega \hat{a}_j^\dagger(\omega)\hat{a}_j(\omega), \tag{2.9}$$

and the positive-frequency field operator becomes

$$\hat{\mathbf{E}}_j^{(+)}(\vec{\mathbf{r}},t) = \int \mathrm{d}\omega \mathcal{E}_j \vec{\mathbf{e}}_j \hat{a}_j(\omega) e^{i(\vec{\mathbf{k}}_j \cdot \vec{\mathbf{r}} - \omega t)}. \tag{2.10}$$

Fourier transformation yields the continuous-mode operators in the time domain, [25]

$$\begin{aligned} \hat{a}_j^\dagger(t) &= \frac{1}{\sqrt{2\pi}} \int \mathrm{d}\omega \hat{a}_j^\dagger(\omega) e^{-i\omega t}, \\ \hat{a}_j(t) &= \frac{1}{\sqrt{2\pi}} \int \mathrm{d}\omega \hat{a}_j(\omega) e^{-i\omega t}, \\ \hat{n}_j &= \int \mathrm{d}t \hat{a}_j^\dagger(t)\hat{a}_j(t), \end{aligned} \tag{2.11}$$

with the commutation relation

$$[\hat{a}_j(t), \hat{a}_j^\dagger(t')] = \delta(t - t'). \tag{2.12}$$

To describe experiments with pulsed light, it is convenient to define a photon-wavepacket creation operator [25]

$$\hat{a}_{j,f}^\dagger = \int \mathrm{d}t f_j(t)\hat{a}_j^\dagger(t) = \int \mathrm{d}\omega F_j(\omega)\hat{a}_j^\dagger(\omega), \tag{2.13}$$

where $f_j(t)$ and $F_j(\omega)$ represent the temporal and spectral profile, respectively, of the photon wavepacket, and are normalized according to Eqs. (2.12) and (2.13) [25]

$$\int \mathrm{d}\omega |F_j(\omega)|^2 = \int \mathrm{d}t |f_j(t)|^2 = 1. \tag{2.14}$$

In this case, the positive-frequency component of the field can be written

$$\hat{\mathbf{E}}_j^{(+)}(\vec{\mathbf{r}},t) = \int \mathrm{d}\omega \mathcal{E}_j \vec{\mathbf{e}}_j F_j^*(\omega)\hat{a}_j(\omega)e^{i(\vec{\mathbf{k}}_j\cdot\vec{\mathbf{r}}-\omega t)}. \tag{2.15}$$

Substituting $F_j(\omega) = \delta(\omega - \omega_j)$ into Eq. (2.15) yields the single-mode monochromatic case in Eq. (2.7). If the bandwidth over which $F_j^*(\omega)$ is non-zero is sufficiently narrow compared to the center frequency ω_j, one may make the approximation

$$\hat{\mathbf{E}}_j^{(+)}(\vec{\mathbf{r}},t) \simeq \mathcal{E}_j \vec{\mathbf{e}}_j e^{i(\vec{\mathbf{k}}_j\cdot\vec{\mathbf{r}}-\omega_j t)} \int \mathrm{d}\omega F_j^*(\omega)\hat{a}_j(\omega). \tag{2.16}$$

Time-dependence is incorporated into quantum optics calculations using one of three representations: the Schrödinger picture, the Heisenberg picture, or the Interaction picture. In the Schrödinger picture, the state vector $|\psi^{(\mathrm{S})}(t)\rangle$ is time-dependent but the operators representing observables $\hat{O}^{(\mathrm{s})}$ are independent of time. In the Heisenberg picture, the state vectors $|\psi^{(\mathrm{H})}\rangle$ are time-independent, while the operators $\hat{O}^{(\mathrm{H})}(t)$ depend on time. The Heisenberg picture is often used to describe pulsed experiments where the duration of the pulse is short compared to the temporal resolution of the detectors. In this case it is common to use a time-independent density matrix, which describes the state of the field averaged over the duration of the pulse, and further averaged from pulse to pulse. It may not always be trivial to calculate the average over the pulse duration, but experimentally this is often what is measured given that single-photon detectors are relatively slow in comparison to the duration of ultrafast laser pulses. In the Interaction picture, both the state vectors $|\psi^{(\mathrm{I})}(t)\rangle$ and the operators $\hat{O}^{(\mathrm{I})}(t)$ are allowed to depend on time. The Interaction picture allows the computation of coherences that depend on time delay τ, such as $g^{(2)}(\tau)$. Each of these three representations are used in this book, with the choice of picture based on convenience for a given scenario. The superscript labels (S), (H), and (I) are used here for illustration, but are typically not included elsewhere.

2.2 SOURCE CHARACTERISTICS

2.2.1 State Vector

If the light emitted by a source is in a pure state, it can be described by a state vector. One can write a generalized multi-mode version of the state vector for a quantized electric field in a pure state, at position $\vec{\mathbf{r}}$ and time t, as [25]

$$|\psi(\vec{\mathbf{r}},t)\rangle = \sum_{n_1,n_2,n_3,\ldots} c_{n_1,n_2,n_3,\ldots}(\vec{\mathbf{r}},t)|n_1\rangle_1|n_2\rangle_2|n_3\rangle_3\ldots, \tag{2.17}$$

where $c_{n_1,n_2,n_3,\ldots}(\vec{\mathbf{r}},t)$ is the complex coefficient of the multi-mode number state ket representing n_1 photons in mode 1, n_2 photons in mode 2, and so on.

This ket can be written as [15]

$$|n_1\rangle_1|n_2\rangle_2|n_3\rangle_3\cdots = \prod_{j=1,2,3,\ldots} \frac{(\hat{a}_j^\dagger)^{n_j}}{\sqrt{n_j!}}|0\rangle, \tag{2.18}$$

where $|0\rangle$ is the global vacuum, representing no photons in any mode. The infinite set of these multi-mode number states form a complete orthonormal set of basis states, so that [25]

$$[\hat{a}_j, \hat{a}_k^\dagger] = \delta_{j,k}. \tag{2.19}$$

In many situations treated in this book, only one mode contains any photons, so the representation of the state can be simplified greatly. In the single-mode case, we can write

$$|\psi(\vec{\mathbf{r}},t)\rangle = \sum_{n=0}^{\infty} c_n(\vec{\mathbf{r}},t)|n\rangle, \tag{2.20}$$

where we have dropped the mode subscript j on the number state. If the state vector does not depend on r or t over the region of interest, or if the information about time- and space-dependence is incorporated into the definition of the mode, we can use the simplified notation

$$|\psi\rangle = \sum_{n=0}^{\infty} c_n|n\rangle. \tag{2.21}$$

In this case an *ideal* single-photon source will emit light in the state

$$|\psi\rangle = |1\rangle, \tag{2.22}$$

which contains exactly one photon in exactly one optical mode.

2.2.2 Density Matrix and Photon Number Probabilities

A more general quantum representation of a state is the density matrix, which is valid for both pure and mixed states. The density-matrix operator for a mixed state can be written as an ensemble average of pure states,

$$\hat{\rho} = \sum_i p_i|\psi_i\rangle\langle\psi_i|, \tag{2.23}$$

where p_i is the probability that the light field occupies state $|\psi_i\rangle$. For a pure state, only one of the coefficients p_i is non-zero, and is equal to one. The ensemble average of an observable $\hat{O}$ can be found from the trace of its product with the density matrix [25]:

$$\langle\hat{O}\rangle = \mathrm{Tr}\{\hat{\rho}\hat{O}\}. \tag{2.24}$$

When the photon number states are used as basis states, the diagonal elements of $\hat{\rho}$ contain the photon number probabilities,

$$P(n) = \mathrm{Tr}\{\hat{\rho}|n\rangle\langle n|\} = \langle n|\hat{\rho}|n\rangle, \tag{2.25}$$

where $P(n)$ is the probability that a source emits n photons. The photon number probabilities are normalized such that

$$\sum_{n=0}^{\infty} P(n) = \mathrm{Tr}\{\hat{\rho}\} = 1, \tag{2.26}$$

which satisfies the usual density-matrix normalization condition.

The notation $P(n > m)$ refers to the total probability that a source emits more than m photons

$$P(n > m) = \sum_{n=m+1}^{\infty} P(n). \tag{2.27}$$

The probability of multi-photon emission, $P(n > 1)$, is a special case of this:

$$P(n > 1) = \sum_{n=2}^{\infty} P(n). \tag{2.28}$$

For a pulsed source, $P(n)$ indicates the probability that the source emits n photons per pulse. The mean number of photons per pulse is

$$\mu = \mathrm{Tr}\{\hat{\rho}\hat{n}\}. \tag{2.29}$$

For typical photon sources, if $P(1) \gg P(n > 1)$, then it is usually the case that $\mu \simeq P(1)$.

For a continuous-wave (CW) source we define $P(n; T)$ as the probability that the source emits n photons in a time interval T, and $\mu(T)$ as the mean number of photons present over the same interval. If $P(1; T) \gg P(n > 1; T)$, then for typical sources $\mu(T) \simeq P(1; T)$. Care should be taken when choosing T, as there can be ambiguity in whether a source emits n photons simultaneously or in succession over the duration of T. This will be discussed in more detail in Section 2.2.5.

2.2.3 Purity

In many applications, particularly those that require indistinguishable photons, it is important that photons be emitted in pure states. The purity of a state can be quantified as

$$\mathcal{P} = \mathrm{Tr}\{\hat{\rho}^2\}. \tag{2.30}$$

Purity has an upper limit of unity for a pure state and a lower limit of $1/N$ for a completely mixed N-dimensional state. A simple example of a mixed state is a pulsed source whose state vector varies from pulse to pulse. If the variation is small, $\mathcal{P}$ may be approximately unity.

2.2.4 Source Efficiency and Generation Rate

For a pulsed source, the source efficiency η_{source} is defined as the probability that the source delivers one or more photons to an experiment for each pump pulse:

$$\eta_{\text{source}} = P(n > 0). \tag{2.31}$$

When characterizing a source, the experiment is often simply a detector or detection system (see Fig. 2.1). In the limit of low multi-photon probability, $P(1) \gg P(n > 1)$, the source efficiency can be estimated from the detected count rate and the detection efficiency as

$$\eta_{\text{source}} \simeq P(1) \simeq \frac{R_{\text{detect}}^{\text{correct}}}{\eta_{\text{DE}} R_{\text{pump}}}, \tag{2.32}$$

where η_{DE} is the detection efficiency defined in Section 2.3.1, R_{pump} is the repetition rate of the electrical or optical pump, and $R_{\text{detect}}^{\text{correct}}$ is the detected count rate, corrected as necessary to account for detector nonidealities such as dark counts, dead time, afterpulsing and differing response to single photons as compared to multiple photons. These corrections, which may or may not be important depending on the specific source and detector involved, are discussed in Chapter 8.

In some cases, it may be possible to decompose the source efficiency into two components,

$$\eta_{\text{source}} = \eta_{\text{gen}} \eta_{\text{extract}}, \tag{2.33}$$

where η_{gen} is the generation efficiency of the source itself and η_{extract} is the extraction efficiency. The generation efficiency is the probability that one or more photons are created within the source per pump pulse. The extraction efficiency includes all optical losses incurred in extracting the photons from where they are generated to where they are useful for an application. This can

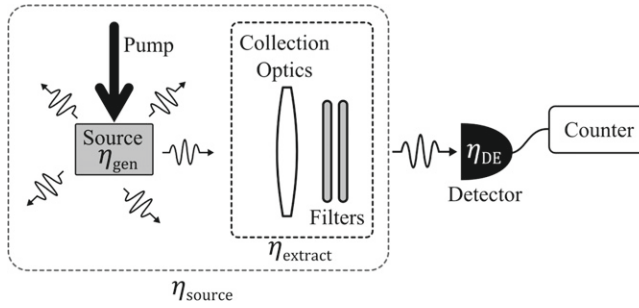

FIGURE 2.1 Schematic showing how the source efficiency, η_{source}, is defined for a pulsed source: as the total probability that a source can deliver one or more photons to an experiment for each pump pulse. In the case shown here, the "experiment" is simply a single-photon detector and a counter. The source efficiency is the product of the generation efficiency of the source itself, η_{gen}, with the efficiency with which photons are extracted from the source and delivered to the detector, η_{extract}.

include losses due to spectral filtering for defining the emission bandwidth and the rejection of any pump light, spatial filtering, geometric alignment, and beam shaping optics. Extraction efficiency is often characterized by measuring transmittance and mode overlap. If η_{gen} and η_{extract} are identified, their dependence on collection optics, spectral bandwidth of filters, pump power, and other critical parameters such as the physical interaction volume defined by the collection should also be given.

A pulsed source may also be characterized by the maximum repetition rate at which it could deliver photons to an experiment, $R_{\text{rep}}^{\text{max}}$. If $R_{\text{rep}}^{\text{max}}$ is identified, any effects that increased rate has on other characteristics, such as the multi-photon emission probability, should also be identified.

For a CW source, the generation rate R_{gen} is typically a more relevant quantity than efficiency. R_{gen} is the total rate at which photons are delivered to a detector, corrected, as in the pulsed case, for detection efficiency and other detector non-idealities:

$$R_{\text{gen}} = \frac{R_{\text{detect}}^{\text{correct}}}{\eta_{\text{DE}}}. \tag{2.34}$$

2.2.5 Second-Order Coherence, $g^{(2)}$

The second-order coherence, $g^{(2)}$, is by far the most common measurement used for determining the quality of a single-photon source, because it gives information about the source's multi-photon emission probability. $g^{(2)}$ is also referred to as the second-order correlation function or the normalized intensity correlation. The second-order coherence between mode j, measured at position $\overrightarrow{\mathbf{r}_1}$ and time t_1, and mode k, measured at position $\overrightarrow{\mathbf{r}_2}$ and time t_2 is [25]

$$g_{j,k}^{(2)}(\overrightarrow{\mathbf{r}_1},t_1;\overrightarrow{\mathbf{r}_2},t_2) = \frac{\langle \hat{\mathbf{E}}_j^{(-)}(\overrightarrow{\mathbf{r}_1},t_1)\hat{\mathbf{E}}_k^{(-)}(\overrightarrow{\mathbf{r}_2},t_2)\hat{\mathbf{E}}_k^{(+)}(\overrightarrow{\mathbf{r}_2},t_2)\hat{\mathbf{E}}_j^{(+)}(\overrightarrow{\mathbf{r}_1},t_1)\rangle}{\langle \hat{\mathbf{E}}_j^{(-)}(\overrightarrow{\mathbf{r}_1},t_1)\hat{\mathbf{E}}_j^{(+)}(\overrightarrow{\mathbf{r}_1},t_1)\rangle\langle \hat{\mathbf{E}}_k^{(-)}(\overrightarrow{\mathbf{r}_2},t_2)\hat{\mathbf{E}}_k^{(+)}(\overrightarrow{\mathbf{r}_2},t_2)\rangle}, \tag{2.35}$$

where the angled brackets denote an ensemble average; in a laboratory experiment, this typically entails an average over a large number of detected photons. Writing in terms of creation and annihilation operators, and cancelling common factors in the numerator and denominator, this becomes

$$g_{j,k}^{(2)}(\overrightarrow{\mathbf{r}_1},t_1;\overrightarrow{\mathbf{r}_2},t_2) = \frac{\langle \hat{a}_j^{\dagger}(\overrightarrow{\mathbf{r}_1},t_1)\hat{a}_k^{\dagger}(\overrightarrow{\mathbf{r}_2},t_2)\hat{a}_k(\overrightarrow{\mathbf{r}_2},t_2)\hat{a}_j(\overrightarrow{\mathbf{r}_1},t_1)\rangle}{\langle \hat{a}_j^{\dagger}(\overrightarrow{\mathbf{r}_1},t_1)\hat{a}_j(\overrightarrow{\mathbf{r}_1},t_1)\rangle\langle \hat{a}_k^{\dagger}(\overrightarrow{\mathbf{r}_2},t_2)\hat{a}_k(\overrightarrow{\mathbf{r}_2},t_2)\rangle}. \tag{2.36}$$

For measurements on a single mode ($j = k$), the j and k subscripts are typically omitted.

This can be written more compactly for a stationary source—one whose properties depend on a time delay $\tau = t_2 - t_1$ but not on specific values of t_1 and t_2. Stable CW sources are typically stationary, whereas pulsed sources are inherently not stationary. For a single-mode, stationary source measured

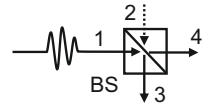

FIGURE 2.2 Illustration of the ports (modes) of an optical beamsplitter (BS). Here an arbitrary field is incident on port 1, and the vacuum field is incident on port 2. For a BS with a field reflection coefficient $\mathcal{R}$ and field transmission coefficient $\mathcal{T}$, the destruction operators can be related as $\hat{a}_3 = \mathcal{R}\hat{a}_1 + \mathcal{T}\hat{a}_2$ and $\hat{a}_4 = \mathcal{T}\hat{a}_1 + \mathcal{R}\hat{a}_2$.

at a single position ($\vec{\mathbf{r}}_1 = \vec{\mathbf{r}}_2$)—or two positions that can be considered as equivalent—this simplifies to the more familiar form:

$$g^{(2)}(\tau) = \frac{\langle \hat{a}^\dagger(t)\hat{a}^\dagger(t+\tau)\hat{a}(t+\tau)\hat{a}(t)\rangle}{\langle \hat{a}^\dagger(t)\hat{a}(t)\rangle^2}. \tag{2.37}$$

It is tempting to try to express $g^{(2)}(\tau)$ in terms of the time-dependent number operator, $\hat{n}(t) = \hat{a}^\dagger(t)\hat{a}(t)$. However, because $\hat{a}$ and $\hat{a}^\dagger$ do not commute, the normally ordered operators in this expression *cannot* be rearranged and

$$g^{(2)}(\tau) \neq \frac{\langle \hat{n}(t)\hat{n}(t+\tau)\rangle}{\langle \hat{n}(t)\rangle^2}. \tag{2.38}$$

In the special case of $\tau = 0$, on the other hand, it is possible to write $g^{(2)}$ in terms of $\hat{n}(t)$ as [25]

$$g^{(2)}(0) = \frac{\langle \hat{n}(t)(\hat{n}(t)-1)\rangle}{\langle \hat{n}(t)\rangle^2}. \tag{2.39}$$

Fortunately, this zero-delay value is typically the most relevant for characterizing a single-photon source. Using this expression, $g^{(2)}(0)$ can be related to the photon number probabilities $P(n)$; this will be discussed in the next section.

One important property of $g^{(2)}(\tau)$ for a light source is that its value does not change with loss as long as all modes experience the same loss. To show this, one need only verify that transmission through a beamsplitter (BS) does not change the second-order coherence, since loss can be modeled as transmission through a lossless BS with arbitrary reflectance and transmittance [26]. An example of such a BS is shown in Fig. 2.2. The input and output destruction operators can be related as [25]

$$\begin{aligned} \hat{a}_3 &= \mathcal{R}\hat{a}_1 + \mathcal{T}\hat{a}_2, \\ \hat{a}_4 &= \mathcal{T}\hat{a}_1 + \mathcal{R}\hat{a}_2. \end{aligned} \tag{2.40}$$

The electric-field reflection and transmission coefficients, $\mathcal{R}$ and $\mathcal{T}$, are complex numbers that satisfy $|\mathcal{R}|^2 + |\mathcal{T}|^2 = 1$ and $\mathcal{R}\mathcal{T}^* + \mathcal{T}\mathcal{R}^* = 1$ for a lossless symmetric BS. For an arbitrary field input at port 1 and a vacuum field input at port 2, one can readily show that [25]

$$g^{(2)}_{44}(\tau) = \frac{|\mathcal{T}|^4\langle \hat{a}_1^\dagger(t)\hat{a}_1^\dagger(t+\tau)\hat{a}_1(t+\tau)\hat{a}_1(t)\rangle}{|\mathcal{T}|^2\langle \hat{a}_1^\dagger(t)\hat{a}_1(t)\rangle|\mathcal{T}|^2\langle \hat{a}_1^\dagger(t+\tau)\hat{a}_1(t+\tau)\rangle}. \tag{2.41}$$

with a similar expression for $g_{33}^{(2)}(\tau)$. Thus the second-order coherence of the transmitted and reflected fields is equal to that of the incident light [25]:

$$g_{11}^{(2)}(\tau) = g_{33}^{(2)}(\tau) = g_{44}^{(2)}(\tau). \tag{2.42}$$

As a result, $g^{(2)}(\tau)$ can be measured accurately in an optical system that has low transmission or low extraction efficiency.

2.2.6 Relating $g^{(2)}$ to $P(n)$

To gain more insight into the information contained in the second-order coherence it is useful to see how it can be related to the photon number probabilities. Here we examine this relationship for both pulsed and CW sources.

2.2.6.1 Pulsed Sources

Pulsed sources are inherently not stationary, and Eq. (2.37) is not valid. In this case, it can be convenient to define a discrete version of $g^{(2)}$ [40]

$$g^{(2)}[m] = \frac{\langle \hat{a}^\dagger[l]\hat{a}^\dagger[l+m]\hat{a}[l+m]\hat{a}[l]\rangle}{\langle \hat{a}^\dagger[l]\hat{a}[l]\rangle\langle \hat{a}^\dagger[l+m]\hat{a}[l+m]\rangle}, \tag{2.43}$$

where l and m take on integer values denoting pulse number, and the angled brackets indicate an average over l. Thus $g^{(2)}[0]$ is the autocorrelation of the pulse train, while $g^{(2)}$ [1] is the cross-correlation of each pulse with its nearest subsequent neighbor (see Fig. 2.3).

In this chapter, square brackets are used to distinguish the discrete form $g^{(2)}[\mathrm{m}]$, valid for pulsed sources, from the continuous form $g^{(2)}(\tau)$, valid for CW sources. In the discrete notation, $g^{(2)}[0]$ is the relevant metric for quantifying the multi-photon emission probability of pulsed single-photon sources, while $g^{(2)}(0)$ is relevant for continuously pumped sources. The remaining chapters of this book drop this distinction and follow the usual convention of using the notation $g^{(2)}(0)$ to characterize both pulsed and CW sources.

The zero-delay value can be written as

$$g^{(2)}[0] = \frac{\langle \hat{n}(\hat{n}-1)\rangle}{\langle \hat{n}\rangle^2}, \tag{2.44}$$

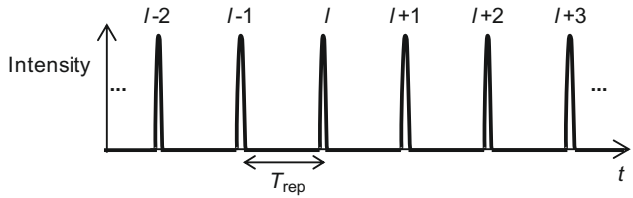

FIGURE 2.3 Optical pulse train illustrating the labeling scheme used in the discrete notation. T_{rep} is the repetition time of the system, which is typically set by the repetition time of the optical or electrical pump.

where the number operator $\hat{n} = \hat{a}^{\dagger}[l]\hat{a}[l]$ measures the number of photons in the lth pulse. The expectation values can be rewritten in terms of the density matrix as

$$g^{(2)}[0] = \frac{\mathrm{Tr}\{\hat{\rho}\hat{n}(\hat{n}-1)\}}{(\mathrm{Tr}\{\hat{\rho}\hat{n}\})^2}. \tag{2.45}$$

Only the diagonal terms of the density matrix (when written in the photon-number-state basis) contribute to $g^{(2)}[0]$. Thus we can rewrite this in terms of the per-pulse photon probabilities as

$$\begin{aligned} g^{(2)}[0] &= \frac{\sum_{n=0}^{\infty} n(n-1)P(n)}{[\sum_{n=0}^{\infty} nP(n)]^2} \\ &= \frac{2P(2)+6P(3)+12P(4)+\cdots}{[P(1)+2P(2)+3P(3)+\cdots]^2} \\ &= \frac{2P(2)+6P(3)+12P(4)+\cdots}{\mu^2}, \end{aligned} \tag{2.46}$$

where μ is the mean photon number per pulse. This expression can be used to bound the probability of multi-photon events by relating this probability to the numerator of $g^{(2)}[0]$ as [8,45]

$$P(n>1) = \sum_{n=2}^{\infty} P(n) \leq \frac{1}{2}\sum_{n=0}^{\infty} n(n-1)P(n). \tag{2.47}$$

As a result, a measured $g^{(2)}[0]$ can be used to place an upper limit on the multi-photon probability:

$$P(n>1) \leq \frac{1}{2}\mu^2 g^{(2)}[0]. \tag{2.48}$$

If $P(2) \gg P(n>2)$, Eq. (2.46) can be approximated as

$$g^{(2)}[0] \simeq \frac{2P(2)}{\mu^2}. \tag{2.49}$$

In the special case where $P(1) \gg P(2) \gg P(n>2)$, which holds for many low-efficiency sources, this simplifies to

$$g^{(2)}[0] \simeq \frac{2P(2)}{[P(1)]^2}. \tag{2.50}$$

Note that $g^{(2)}[0]$ does not directly reflect the two:one photon ratio $P(2)/P(1)$, as one might naively expect. Although $g^{(2)}[0]$ is the most commonly cited metric of single-photon source quality, for some applications $P(2)/P(1)$ is the more relevant quantity.

The discussion above assumes each pulse is treated as a whole, and photon statistics are averaged over the pulse duration. More information about a source can be obtained by studying the detailed time evolution of $g^{(2)}$ during each pulse [1,12].

2.2.6.2 CW Sources

If $P(1;T) \gg P(2;T) \gg P(n>2;T)$ for a time interval T over which $g^{(2)}(\tau)$ is approximately equal to the zero-delay value (*i.e.*, $g^{(2)}(T) \simeq g^{(2)}(0)$), then this can be approximated as

$$g^{(2)}(0) \simeq \frac{2P(2;T)}{[P(1;T)]^2}. \tag{2.51}$$

Care should be taken when choosing T, given that a source may be able to emit two photons simultaneously or in succession.

To illustrate this point, it is useful to consider an example. Suppose we have an approximation to a single-photon source that emits photons at a rate $R_{\text{gen}} = 10^6\ \text{s}^{-1}$ and has the $g^{(2)}(\tau)$ shown in Fig. 2.4, where $g^{(2)}(0) = 0.1$ and $g^{(2)}(\tau)$ is approximately constant over a time delay range >1 ns about the origin, as shown in Fig. 2.4b. Thus, over a time interval $T = 1$ ns, the probability of the source emitting one or more photons is

$$P(n>0;\,1\text{ ns}) = 10^{-9}\ \text{s} \times 10^6\ \text{s}^{-1} = 10^{-3}. \tag{2.52}$$

Given this very low probability, we can make the approximation $P(1;\,1\text{ ns}) \simeq P(n>0;\,1\text{ ns})$. Solving Eq. (2.51) for the two-photon probability over a 1 ns interval yields

$$P(2;\,1\text{ ns}) \simeq \frac{1}{2}g^{(2)}(0)[P(1;\,1\text{ ns})]^2. \tag{2.53}$$

Using the numbers for this example source, we find

$$P(2;\,1\text{ ns}) \simeq 5 \times 10^{-8}. \tag{2.54}$$

The two:one photon ratio in this case is

$$\frac{P(2;\,1\text{ ns})}{P(1;\,1\text{ ns})} \simeq 5 \times 10^{-5}. \tag{2.55}$$

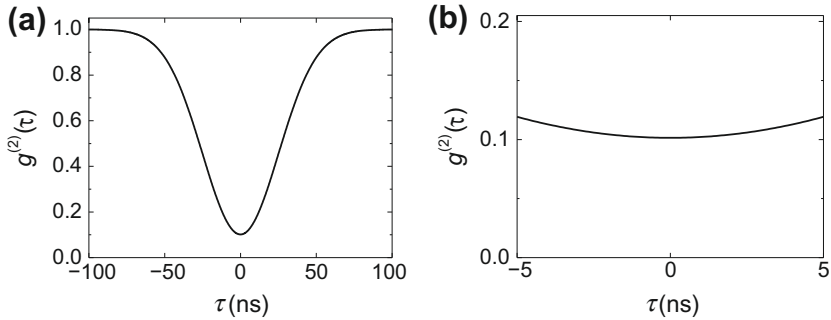

FIGURE 2.4 Second-order coherence of the example non-ideal single-photon source discussed in the text. Plot (b) is a close-up view near zero delay of the data in (a).

By contrast, a source with Poissonian photon statistics and the same generation rate would have

$$P(2;\,1\text{ ns}) \simeq 5 \times 10^{-7} \tag{2.56}$$

and

$$\frac{P(2;\,1\text{ ns})}{P(1;\,1\text{ ns})} \simeq 5 \times 10^{-4}. \tag{2.57}$$

The two:one photon ratio is an order of magnitude worse in the latter case, although neither is particularly large when considering such a short time duration. Judging from the width of the antibunching dip, however, the photons emitted by this source are likely to have wavepacket envelopes with durations much longer than 1 ns, leading to much higher two-photon probabilities. Calculations over time scales where $g^{(2)}(\tau)$ is not constant are outside the scope of the simple treatment outlined here.

2.2.7 Ideal and Non-Ideal Single-Photon Sources

As mentioned in Sections 2.2.1 and 2.2.4, an ideal single-photon source will emit exactly one photon into a well-defined optical mode that can be efficiently collected and delivered to an experiment. Two important and distinct features of an ideal source are: (1) it never emits more than one photon at a time, and (2) it emits single photons with unity source efficiency. An ideal pulsed source thus has $\eta_{\text{source}} = 1$ and $g^{(2)}[0] = 0$. For an ideal CW source, the generation rate is limited only by the temporal duration of each photon wavepacket (often referred to as temporal coherence) and $g^{(2)}(0) = 0$, with $g^{(2)}(\tau) \to 1$ as $\tau \to \infty$.

To illustrate the distinction between these two features, consider a non-ideal source in the form of a pulsed source that never emits two or more photons in the same pulse, yet has $\eta_{\text{source}} < 1$. Such a source could emit light into the pure state

$$|\psi\rangle = \sqrt{P(0)}|0\rangle + \sqrt{P(1)}|1\rangle, \tag{2.58}$$

or the mixed state

$$\hat{\rho} = P(0)|0\rangle\langle 0| + P(1)|1\rangle\langle 1|. \tag{2.59}$$

The multi-photon emission probability of either source is zero,

$$P(n > 1) = 0, \tag{2.60}$$

as is the second-order coherence at zero delay,

$$g^{(2)}[0] = 0. \tag{2.61}$$

The source efficiency, mean photon number, and probability of one-photon emission are all equal:

$$\eta_{\text{source}} = \mu = P(1). \tag{2.62}$$

In practice, no single-photon source is ideal in all ways—yet much can be done with non-ideal sources. To determine whether a source is useful

in a given application it is necessary to establish whether the multi-photon emission probabilities are sufficiently small and whether the source efficiency (or generation rate) is sufficiently large for that application.

2.2.8 To measure $P(n)$ or $g^{(2)}$?

It might seem that measuring the photon number distribution $P(n)$ would be the most direct way to characterize a single-photon source. One could then compare the single-photon probability $P(1)$ with the multi-photon probabilities $P(2), P(3)$, etc. Photon-number-resolving detectors do exist (they are discussed in Section 2.3 and in subsequent chapters); to date, however, even the best devices do not yet combine very high efficiency with low timing jitter and short dead times [31,46,27]. Unless the detection efficiency of a number-resolving detector is 100%, the measured photon statistics will be skewed by loss. In principle, the loss matrix can be inverted to reconstruct the statistics of the optical state [46,27,5], but such an inversion works best with efficiencies as high as possible. By contrast, $g^{(2)}$ can be measured accurately even with click/no-click detectors with low detection efficiencies. This is one of the key reasons that $g^{(2)}$ is used to characterize the vast majority of single-photon sources.

2.2.9 Hanbury Brown-Twiss Interferometer

Typically, $g^{(2)}(\tau)$ is measured with a Hanbury Brown-Twiss (HBT) interferometer [19], such as the one shown in Fig. 2.5. This consists of a beamsplitter, two discrete single-photon detectors, and some form of timing or coincidence electronics. An incoming optical field in mode 1 is divided at the beamsplitter and sent to two output ports, modes 3 and 4, which are incident on two detectors, D_3 and D_4. One can appreciate how the HBT interferometer works qualitatively for an ideal single-photon source: if only one photon at a time is input in mode 1, there is no way for both detectors D_3 and D_4 to detect a photon simultaneously, and $g^{(2)}(0) = 0$.

The timing electronics record the relative time delay between the two detection events at D_3 and D_4. In the original HBT experiment [19], and for many years thereafter, the timing electronics consisted of a simple start-stop

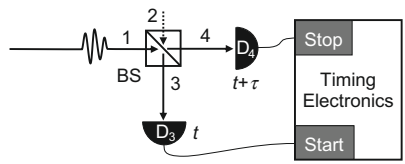

FIGURE 2.5 Hanbury Brown-Twiss interferometer. The light field to be measured is incident on input port 1 of the beamsplitter (BS), while a vacuum field is incident on input port 2. With appropriate normalization, a histogram of the correlations between photon numbers measured by detectors at output ports 3 and 4 can yield a good approximation to $g^{(2)}(\tau)$.

timing circuit. In this case, the timer starts when detector D_3 registers a photon and stops after a time delay τ, when detector D_4 records a photon. The timing electronics record a histogram of these start-stop delay times that is ideally proportional to $g^{(2)}(\tau)$. It is not critical that the optical path length from the BS to D_3 is equal to that from the BS to D_4, as any difference in photon arrival time can be compensated by changing the length of electrical cables or adjusting internal delays in the electronics. In the case of a simple start-stop timer, the stop pulse is often purposely delayed from the start, so that negative delay data ($\tau < 0$) can be recorded. In recent years, more sophisticated electronics have been employed. For example, time-tagging electronics can record the arrival times of all detected photons and data can be post-processed to form multi-start, multi-stop correlation histograms that more accurately resemble $g^{(2)}(\tau)$, especially at higher count rates.

In the remainder of this section we examine the HBT interferometer more quantitatively and explore how well real HBT experiments recover $g^{(2)}(\tau)$.

2.2.9.1 HBT with Photon-Number-Resolving Detectors

If D_3 and D_4 are ideal photon-number-resolving detectors with unity detection efficiency, they can accurately measure $\hat{n}_3(t)$, the number of photons in mode 3 at time t, and $\hat{n}_4(t+\tau)$, the number of photons in mode 4 at time $t+\tau$. Such detectors could be used to obtain a normalized correlation between the photon numbers in the two outputs,

$$\gamma^{(2)}_{\mathrm{PNR}}(\tau) = \frac{\langle \hat{n}_3(t)\hat{n}_4(t+\tau)\rangle}{\langle \hat{n}_3(t)\rangle\langle \hat{n}_4(t+\tau)\rangle}, \tag{2.63}$$

where the subscript PNR denotes the use of photon-number-resolving detectors. Given that $[\hat{a}_3, \hat{a}_4^\dagger] = 0$, the operators in the numerator can be rearranged to show that this correlation is equal to the second-order coherence between these two modes [13,25]:

$$\gamma^{(2)}_{\mathrm{PNR}}(\tau) = \frac{\langle \hat{a}_3^\dagger(t)\hat{a}_4^\dagger(t+\tau)\hat{a}_4(t+\tau)\hat{a}_3(t)\rangle}{\langle \hat{a}_3^\dagger(t)\hat{a}_3(t)\rangle\langle \hat{a}_4^\dagger(t+\tau)\hat{a}_4(t+\tau)\rangle} = g^{(2)}_{34}(\tau), \tag{2.64}$$

Using the beamsplitter transformations in Eq. (2.40) one can show that the measured photon number correlation between D_3 and D_4 is exactly equal to the second-order coherence of the incident light:

$$\gamma^{(2)}_{\mathrm{PNR}}(\tau) = \frac{|\mathcal{R}|^2|\mathcal{T}|^2\langle \hat{a}_1^\dagger(t)\hat{a}_1^\dagger(t+\tau)\hat{a}_1(t+\tau)\hat{a}_1(t)\rangle}{|\mathcal{R}|^2\langle \hat{a}_1^\dagger(t)\hat{a}_1(t)\rangle|\mathcal{T}|^2\langle \hat{a}_1^\dagger(t+\tau)\hat{a}_1(t+\tau)\rangle} = g^{(2)}_{11}(\tau). \tag{2.65}$$

So far we have assumed 100% detection efficiency, but we can relax this requirement and still recover $g^{(2)}_{11}(\tau)$ exactly. To show this, we model the detection efficiencies, η_3 and η_4, as a beamsplitter with transmittance η_3 in front

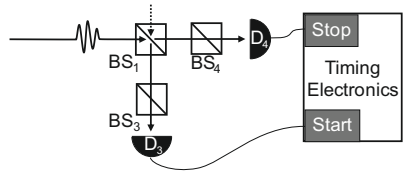

FIGURE 2.6 Model of a Hanbury Brown-Twiss interferometer employing detectors with non-unity detection efficiency. The detection efficiency of the detectors in modes 3 and 4 are taken to be η_3 and η_4. These efficiencies are modeled here as beamsplitters BS_3 and BS_4, with transmission coefficient $\mathcal{T}_3 = \sqrt{\eta_3}$ and $\mathcal{T}_4 = \sqrt{\eta_4}$, followed by detectors D_3 and D_4, respectively. D_3 and D_4 are both modeled as ideal photon-number-resolving detectors with $\eta_{DE} = 1$.

of D_3 and a beamsplitter with transmittance η_4 in front of D_4. The normalized correlation between the number of photons *detected* by D_3 and D_4 is also equal to $g^{(2)}(\tau)$ of the incident field [25,26] (see Fig. 2.6).

$$\gamma^{(2)}_{\mathrm{PNR}(\eta_3,\eta_4)}(\tau) = \frac{\eta_3\eta_4\langle\hat{n}_3(t)\hat{n}_4(t+\tau)\rangle}{\eta_3\langle\hat{n}_3(t)\rangle\eta_4\langle\hat{n}_4(t+\tau)\rangle} = g^{(2)}_{11}(\tau). \tag{2.66}$$

2.2.9.2 HBT with "Click" Detectors

Since ideal PNR detectors with sufficient timing resolution are not readily available, HBT interferometers have typically employed single-photon detectors that can be described as "click," or "click/no-click," detectors. Such a detector will give an output response if it detects one or more photons, but has no way of distinguishing two or more photons from one photon. Click detectors are discussed in more detail in Section 2.3.3.

To explore the conditions under which an HBT interferometer with click detectors correctly measures the second-order coherence, we can define the measured temporal correlation function

$$\gamma^{(2)}_{\mathrm{click}}(\tau) \equiv \left\langle \frac{p_{3,4}(\mathrm{click}(t),\mathrm{click}(t+\tau))}{p_3(\mathrm{click}(t))\,p_4(\mathrm{click}(t+\tau))} \right\rangle, \tag{2.67}$$

where $p_{3,4}(\mathrm{click}(t),\mathrm{click}(t+\tau))$ is the probability that detector 3 clicks at time t and detector 4 clicks at time $t+\tau$; $p_3(\mathrm{click}(t))$ is the probability that detector 3 clicks at time t; $p_4(\mathrm{click}(t+\tau))$ is the probability that detector 4 clicks at time $t+\tau$; and the average is taken over all time t. We can estimate this quantity from measurements by using

$$\hat{\gamma}^{(2)}_{\mathrm{click}}(\tau) = \frac{N_c(\tau;\Delta\tau)}{R_3R_4\Delta\tau T_{\mathrm{int}}}, \tag{2.68}$$

where $N_c(\tau;\Delta\tau)$ is the number of correlation events recorded by the timing electronics in the histogram bin centered at delay τ having width $\Delta\tau$. This quantity represents the number of times that a click on detector 3 is followed by a click on detector 4 after a delay ranging from $\tau - \Delta\tau/2$ to $\tau + \Delta\tau/2$. R_3 and

R_4 are the singles count rates on detectors D_3 and D_4, and T_{int} is the integration time or experiment run time. For a CW source, $\Delta\tau$ is often set at the minimum value allowed by the timing resolution of the detectors and electronics, but in some cases a wider bin can be chosen if $g^{(2)}(\tau)$ evolves more slowly with τ.

For pulsed sources, the measured correlation function can be normalized to find the area of each pulse in the histogram as

$$\hat{\gamma}^{(2)}_{\text{click}}[m] = \frac{N_c[m]}{R_3 R_4 T_{\text{rep}} T_{\text{int}}}, \tag{2.69}$$

where m takes on integer values and $\Delta\tau$ has been replaced by the pump repetition period T_{rep}. Assuming a lossless BS with arbitrary $\mathcal{R}$ and $\mathcal{T}$ and click detectors with detection efficiencies η_3 and η_4, the pulsed measurement outcome at zero delay can be written as a function of the photon probability distribution of the incident light by computing the joint probability distribution of photons detected by D_3 and D_4 [44].

In general, $\gamma^{(2)}_{\text{click}}[0]$ is not equal to $g^{(2)}[0]$, but under appropriate experimental conditions $\gamma^{(2)}_{\text{click}}[0]$ can approximate $g^{(2)}[0]$ quite well. It is illustrative to write out the first few terms of each factor in the numerator and denominator [44]:

$$\gamma^{(2)}_{\text{click}}[0] = \frac{\eta_3\eta_4|\mathcal{R}|^2|\mathcal{T}|^2\left[2P(2)+6P(3)\left(1-\frac{1}{2}\eta_3|\mathcal{R}|^2-\frac{1}{2}\eta_4|\mathcal{T}|^2\right)+\cdots\right]}{\eta_3|\mathcal{R}|^2\left[P(1)+2P(2)\left(1-\frac{1}{2}\eta_3|\mathcal{R}|^2\right)+\cdots\right]\eta_4|\mathcal{T}|^2\left[P(1)+2P(2)\left(1-\frac{1}{2}\eta_4|\mathcal{T}|^2\right)+\cdots\right]} \tag{2.70}$$

where the $P(n)$'s represent the photon number probability distribution of the light input in mode 1. If we keep just the lowest order terms in Eq. (2.70), we can see that it reduces to Eq. (2.50). For higher photon numbers, $\mathcal{R}, \mathcal{T}, \eta_3$, and η_4 appear as correction factors, indicating that the higher photon number terms tend to be underestimated by the click detectors. In the limit of very low detection efficiencies, these corrections to the higher photon number terms become negligible. Applying l'Hôpital's rule to Eq. (2.70) yields

$$\lim_{\eta_3,\eta_4\to 0} \gamma^{(2)}_{\text{click}}[0] = g^{(2)}[0], \tag{2.71}$$

regardless of the values of $\mathcal{R}$ and $\mathcal{T}$. Alternatively, if the source has very low multi-photon generation probabilities so that $P(1) \gg P(2) \gg P(n>2)$, then

$$\gamma^{(2)}_{\text{click}}[0] \simeq \frac{2P(2)}{[P(1)]^2} \simeq g^{(2)}[0]. \tag{2.72}$$

Although the coincidence probability is maximized for $\mathcal{R} = \mathcal{T} = 1/2$, because of the way $\gamma^{(2)}_{\text{click}}[0]$ is normalized, it can still give a good approximation to $g^{(2)}[0]$ even when $\mathcal{R} \neq \mathcal{T}$ or when the detection efficiencies are not matched, $\eta_3 \neq \eta_4$. Because loss does not change $g^{(2)}$, even though it alters the photon

probabilities $P(n)$, the measurement fidelity can be improved by introducing additional loss to the system. Care should be taken to ensure that any additional loss is the same for all modes; for example, any additional spatial or spectral filtering should be avoided.

2.2.9.3 *Summary of HBT Interferometry in the Characterization of a Single-Photon Source*

The HBT interferometer has several important properties that make it especially useful for accurate measurements of $g^{(2)}(\tau)$.

(1) The BS reflectance:transmittance ratio does not need to be perfectly 50:50.
(2) The detection efficiencies of D_3 and D_4 do not have to be 100 % or even matched to one another.
(3) Threshold or click detectors can be used without sacrificing accuracy, as long as $P(1) \gg P(2) \gg P(n > 2)$.
(4) Loss does not change $g^{(2)}(\tau)$, so it can be measured accurately even in a system with unknown and potentially large losses.

There are a number of key experimental limitations to the HBT interferometer. For example, if $g^{(2)}(\tau)$ varies significantly over time delays that are short compared to the timing jitter of detectors and/or electronics, then the measured $\gamma^{(2)}(\tau)$ will be a convolution of $g^{(2)}(\tau)$ and an instrument response function. While it may be possible in some cases to deconvolve these two components and obtain a better estimate of the source $g^{(2)}(\tau)$, it is generally not an easy task. In addition, normalizing by count rates, as in Eqs. (2.68) and (2.69), may prove inaccurate if the count rates vary during the acquisition time. In this case, it might be preferable to perform a piece-wise normalization over shorter time intervals, if possible.

Finally, it is worth noting that a beamsplitter is not necessarily required to measure the second-order coherence. Beamsplitters are used chiefly because readily available single-photon detectors have non-zero dead time and a limited ability to resolve photon number. Recent demonstrations have shown that $g^{(2)}(\tau)$ of single- or few-photon states can be measured with one detector, provided that the detector either has a very short dead time [42] or the ability to resolve photon number [51].

2.2.10 Bunching, Antibunching, and Poissonian Photon Statistics

A source exhibits ***bunching*** if photons are more likely to arrive closely spaced in time than they are to arrive further apart. Conversely, a source exhibits ***antibunching*** if photons are more likely to arrive far apart in time than close together. These conditions are typically expressed as $g^{(2)}(0) > g^{(2)}(\tau \neq 0)$ for bunching and $g^{(2)}(0) < g^{(2)}(\tau \neq 0)$ for antibunching [25,50]. (These relations break down for a source that is antibunched over some time scales and bunched over others [48].)

A source with ***Poissonian*** photon number statistics, such as the coherent state discussed in Section 2.2.13, is neither bunched nor antibunched, and has $g^{(2)}(\tau) = 1$ for all τ. In this case photon arrival times are distributed randomly, with two photons displaying no preference for arriving separated by short or long time delays [25,50]. Note however that $g^{(2)}(\tau) = 1$ does not necessarily imply that the photon number distribution follows a Poisson distribution. One example is a statistical mixture of three sources (single-photon, thermal, and coherent) in three modes that can add up in the right proportion to yield $g^{(2)}(\tau) = 1$ and yet have a probability distribution that cannot be described by a Poisson distribution [18].

Nevertheless, it is useful to define terms that delineate how $g^{(2)}$ varies from the value it takes for Poissonian sources. One way of looking at $g^{(2)}$ is as a quantity relating the mean photon number to the magnitude of the variation in photon number. To see this, we can examine the pulsed case and rewrite Eq. (2.44) as [25]

$$g^{(2)}[0] = 1 + \frac{(\Delta n)^2 - \mu}{\mu^2}, \tag{2.73}$$

where $\mu = \langle \hat{n} \rangle$ is the mean photon number and the variance is

$$(\Delta n)^2 = \langle \hat{n}^2 \rangle - \langle \hat{n} \rangle^2. \tag{2.74}$$

Thus $g^{(2)}$ is a measure of the relative magnitude of the mean and the variance. For a Poisson source or any other source with $g^{(2)} = 1$, the mean and variance are equal: $\mu = (\Delta n)^2$. If the variance in photon number is *larger* than the mean, then $g^{(2)} > 1$ and the source exhibits ***super-Poissonian*** behavior. If the variance is *smaller* than the mean, then $g^{(2)} < 1$ and the source exhibits ***sub-Poissonian*** behavior. Because classical light fields are constrained to $g^{(2)} \geq 1$, sub-Poissonian statistics can only be described using a quantized electromagnetic field [17,25].

Because of the timing jitter limitations of detectors and electronics, a measured $\gamma^{(2)}(\tau)$ may not fully capture the fastest temporal dynamics of $g^{(2)}(\tau)$. As a result, measuring $\gamma^{(2)}(0) = 1$ does not necessarily imply that $g^{(2)}(0) = 1$. Most thermal sources, for example, have coherence times far too short ($\ll$1 ps) for the consequent bunching to be resolved in a typical $\gamma^{(2)}(\tau)$ measurement.

Most single-photon-source approximations exhibit both antibunching and sub-Poissonian photon statistics. However, an antibunched source does not necessarily have sub-Poissonian photon statistics [30,48]. One example is a source that exhibits "blinking," displaying antibunching on very short time scales and bunching on longer time scales [4]; an illustrative example of this is plotted in Fig. 2.7b. This highlights the importance of correctly normalizing $\gamma^{(2)}(\tau)$: if such a source is bunched over a much longer time scale than the antibunching (so that the bunching peak looks flat over the measured delay range), then a source may appear to have sub-Poissonian statistics, when in fact $g^{(2)}(\tau) > 1$.

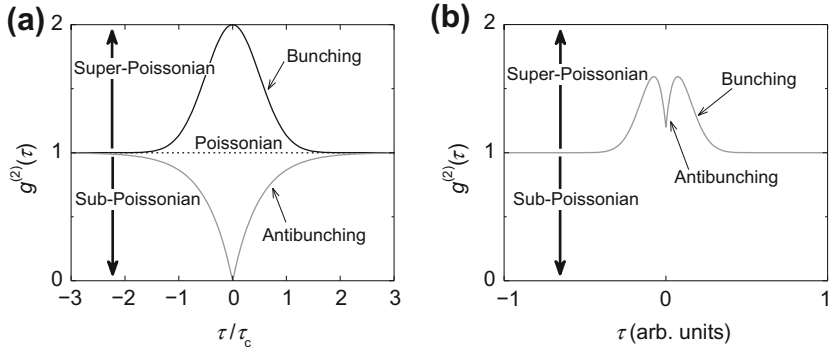

FIGURE 2.7 (a) Plot showing the relationships among bunching, antibunching, sub-, super- and Poissonian photon statistics. Plotted are three ideal sources: a chaotic, thermal-like source (solid black curve), a coherent source (dotted black curve), and a single-photon source (solid gray curve). τ_c is the coherence time of the bunched and antibunched sources. (b) Illustration of how a source could be antibunched without exhibiting sub-Poissonian photon statistics.

Likewise, sub-Poissonian photon statistics do not necessarily imply that a source will be antibunched, although this requires a light source that would be difficult to implement in a practical setting [30,48].

2.2.11 High-Order Coherences

In some cases, it may be relevant to measure coherences higher than second order, given that in principle one needs to know all orders to fully reconstruct the density matrix [17]. The third-order coherence for a single-mode stationary source can be written:

$$g^{(3)}(\tau_1,\tau_2) = \frac{\langle \hat{a}^\dagger(t)\hat{a}^\dagger(t+\tau_1)\hat{a}^\dagger(t+\tau_2)\hat{a}(t+\tau_2)\hat{a}(t+\tau_1)\hat{a}(t)\rangle}{\langle \hat{a}^\dagger(t)\hat{a}(t)\rangle^3}. \quad (2.75)$$

For a pulsed source, we can write a discrete version for the zero-delay value in terms of the density matrix:

$$g^{(3)}[0,0] = \frac{\mathrm{Tr}\{\hat{\rho}\hat{n}(\hat{n}-1)(\hat{n}-2)\}}{(\mathrm{Tr}\{\hat{\rho}\hat{n}\})^3}. \quad (2.76)$$

In terms of photon probabilities, this is

$$\begin{aligned} g^{(3)}[0,0] &= \frac{\sum_{n=0}^{\infty} n(n-1)(n-2)P(n)}{[\sum_{n=0}^{\infty} nP(n)]^3} \\ &= \frac{6P(3)+24P(4)+\cdots}{[P(1)+2P(2)+3P(3)+\cdots]^3} \\ &\simeq \frac{6P(3)}{[P(1)]^3}, \end{aligned} \quad (2.77)$$

where the approximation in the last line holds provided $P(1) \gg P(n > 1)$ and $P(3) \gg P(n > 3)$. The temporal coherence can be generalized to arbitrary order m as

$$g^{(m)}(\vec{\tau}) = \frac{\langle \hat{a}^\dagger(t)[\prod_{i=1}^{m-1}\hat{a}^\dagger(t+\tau_i)][\prod_{i=m-1}^{1}\hat{a}(t+\tau_i)]\hat{a}(t)\rangle}{\langle \hat{a}^\dagger(t)\hat{a}(t)\rangle^m}, \tag{2.78}$$

where $\vec{\tau} = (\tau_1, \tau_2, \ldots, \tau_{m-1})$. The leading-term approximation for a pulsed source when all delays are zero is

$$g^{(m)}[\vec{0}] \simeq \frac{m!P(m)}{[P(1)]^m}, \tag{2.79}$$

assuming $P(1) \gg P(n > 1)$ and $P(m) \gg P(n > m)$. Thus, in sources with low mean photon number, to first order the m^{th}-order coherence will tend to be dominated by the m-photon contribution. For an ideal single-photon source, all $P(n)$ are zero for $n \geq 2$, and so all higher-order coherences are also identically zero.

Because $g^{(2)}(\tau)$ has the form of an autocorrelation, it must be symmetric about τ. Higher-order coherences lack this constraint. It has been proposed that asymmetry in $g^{(3)}(\tau_1, \tau_2)$ can indicate irreversible processes, which could be used to distinguish a non-equilibrium steady state from true equilibrium in chemical reactions, for example [38].

2.2.12 Indistinguishability

As discussed above, while an ideal single-photon source will emit exactly one photon at a time, many applications further require indistinguishability of the emitted photons. This may mean that two or more successive photons from a single source are emitted into identical quantum states. It may also mean that multiple single-photon sources should emit photons that are indistinguishable from one another.

Two photons are perfectly indistinguishable if their density matrices $\hat{\rho}_1$ and $\hat{\rho}_2$ are equal. To quantify the difference between two unequal density matrices, we can define the indistinguishability of these two photons as

$$\mathcal{J}(\hat{\rho}_1, \hat{\rho}_2) = 1 - \frac{1}{2}\|\hat{\rho}_1 - \hat{\rho}_2\|^2, \tag{2.80}$$

where $\|\hat{\rho}_1 - \hat{\rho}_2\|^2$ is the operational distance between $\hat{\rho}_1$ and $\hat{\rho}_2$ [23,35]. This operational distance has a maximum value of two, and $\mathcal{J}(\hat{\rho}_1, \hat{\rho}_2)$ has a minimum value of zero, if $\hat{\rho}_1$ and $\hat{\rho}_2$ are perfectly distinguishable. If $\hat{\rho}_1 = \hat{\rho}_2$, then $\|\hat{\rho}_1 - \hat{\rho}_2\|^2 = 0$ and $\mathcal{J}(\hat{\rho}_1, \hat{\rho}_2) = 1$. If the two input photons are in pure states, then the density matrices can be written as $\hat{\rho}_1 = |\psi_1\rangle\langle\psi_1|$, and $\hat{\rho}_2 = |\psi_2\rangle\langle\psi_2|$, and the indistinguishability is [23,35]

$$\mathcal{J}(\hat{\rho}_1, \hat{\rho}_2) = |\langle\psi_1|\psi_2\rangle|^2. \tag{2.81}$$

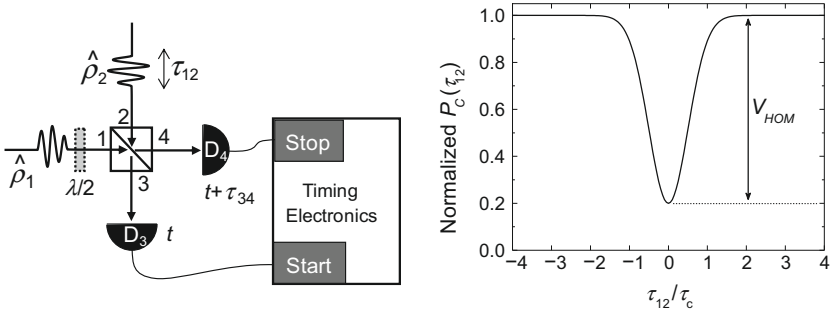

FIGURE 2.8 Left panel: Schematic for measuring HOM interference. The time delay τ_{12} is the elapsed time from when photon 1 arrives at the BS to when photon 2 arrives at the BS. This delay, which can be scanned by adjusting the optical path length of one of the input arms, can be varied in steps much smaller than the timing resolution of the single-photon detectors D_3 and D_4. Alternatively, a half-wave plate ($\lambda/2$) can be inserted into one input port (port 1 here) to rotate the polarization of $\hat{\rho}_1$ so that it is orthogonal to that of $\hat{\rho}_2$, making the two photons perfectly distinguishable. The time delay τ_{34} is the elapsed time from when a photon is detected by D_3 to when a photon is detected by D_4. Coincidences are events where $\tau_{34} = 0$: both D_3 and D_4 detect photons at the same time. Right panel: Theoretical plot of HOM dip for $V_{\text{HOM}} = 0.8$.

This is recognizable as the fidelity [49]. In principle, indistinguishability could be computed by separately measuring all the quantum properties of the two states, including the spectral, temporal, and spatial profiles, and the polarization state, and fully accounting for all measurement bias, such as mode selectivity.

In practice, the indistinguishability of two photons is instead typically quantified by observing Hong-Ou-Mandel (HOM) interference between them [20]. In an HOM interferometer, if two photons are incident on the two input ports of an ideal 50:50 beamsplitter, their paths can interfere such that both photons must exit the same output port of the BS.

A typical experimental setup is shown in Fig. 2.8. If two indistinguishable single photons in pure states are incident on the BS, one each at ports 1 and 2, they transform as $|1\rangle_1|1\rangle_2 \rightarrow (|2\rangle_3|0\rangle_4 + |0\rangle_3|2\rangle_4)/\sqrt{2}$. Both photons could be detected by either detector D_3 or detector D_4, but the probability of a coincidence between the two detectors, P_c, is zero. The visibility of the HOM interferometer is found by comparing this coincidence probability to the coincidence probability when the two input photons are made perfectly distinguishable.

One method of measuring the visibility is to vary the time delay, τ_{12}, between the photons incident to ports 1 and 2. The probability of coincidences (events where $\tau_{34} = 0$) between detected photons in output ports 3 and 4 is measured as a function of this time delay, $P_c(\tau_{12})$. In the ideal case, $P_c(0) = 0$. One can define a visibility [34]

$$V_{\text{HOM}} = \frac{P_c(\tau_{12} \gg \Delta\tau_{\text{dip}}) - P_c(0)}{P_c(\tau_{12} \gg \Delta\tau_{\text{dip}})}, \tag{2.82}$$

where the long-delay limit is measured at a delay τ_{12} much longer than the width of the HOM dip $\Delta\tau_{\text{dip}}$; in other words, the time delay is large enough that the photon wavepackets do not overlap in time.

As an alternative to scanning the delay, if all photons are linearly polarized, a half-wave plate can be inserted into one of the input ports of the beamsplitter. In this way, the two photons can be made perfectly distinguishable by setting the polarizations orthogonal to one another. The measured coincidence probabilities for parallel polarizations, $P_{\text{c}}(||)$, and for orthogonal polarizations, $P_{\text{c}}(\perp)$, can then be used to determine the visibility as [11]

$$V_{\text{HOM}} = \frac{P_{\text{c}}(\perp) - P_{\text{c}}(||)}{P_{\text{c}}(\perp)}. \tag{2.83}$$

The HOM visibility can reach its maximum value of unity only if three conditions are met: (1) there must never be more than one photon in either input port, (2) the two photons must be indistinguishable from one another, and (3) both photons must be in pure states. If there is exactly one photon at each input port and the BS has a 50:50 split ratio, V_{HOM} can be written in terms of the input density matrices $\hat{\rho}_1$ and $\hat{\rho}_2$ as [35]

$$V_{\text{HOM}} = \text{Tr}\{\hat{\rho}_1\hat{\rho}_2\} = \frac{\text{Tr}\{\hat{\rho}_1^2\} + \text{Tr}\{\hat{\rho}_2^2\} - ||\hat{\rho}_1 - \hat{\rho}_2||^2}{2}. \tag{2.84}$$

Because $\text{Tr}\{\hat{\rho}_1^2\} \leq 1$ and $\text{Tr}\{\hat{\rho}_2^2\} \leq 1$, this visibility serves as a lower limit to indistinguishability

$$V_{\text{HOM}} \leq \mathcal{J}(\hat{\rho}_1, \hat{\rho}_2). \tag{2.85}$$

If the two input photons are in pure states $|\psi_1\rangle$ and $|\psi_2\rangle$, then $\text{Tr}\{\hat{\rho}_1^2\} = \text{Tr}\{\hat{\rho}_2^2\} = 1$, and hence the visibility and indistinguishability are equivalent [23,35]:

$$V_{\text{HOM}} = \mathcal{J}(\hat{\rho}_1, \hat{\rho}_2) = |\langle\psi_1|\psi_2\rangle|^2. \tag{2.86}$$

V_{HOM} can be reduced below unity by many mechanisms, including background counts, multi-photon events, and other experimental imperfections. This makes HOM interferometry a powerful tool for identifying any unforeseen imperfections in a source or an experimental setup that need to be addressed.

2.2.13 Other Sources

In addition to single-photon sources, several other sources will be discussed throughout this book, both to highlight the ways they contrast with single-photon sources, and as sources that have important applications in their own rights.

2.2.13.1 Coherent Source

A coherent state is defined as [17]

$$|\alpha\rangle = \exp\left(-\frac{1}{2}|\alpha|^2\right)\sum_{n=0}^{\infty}\frac{\alpha^n}{\sqrt{n!}}|n\rangle. \tag{2.87}$$

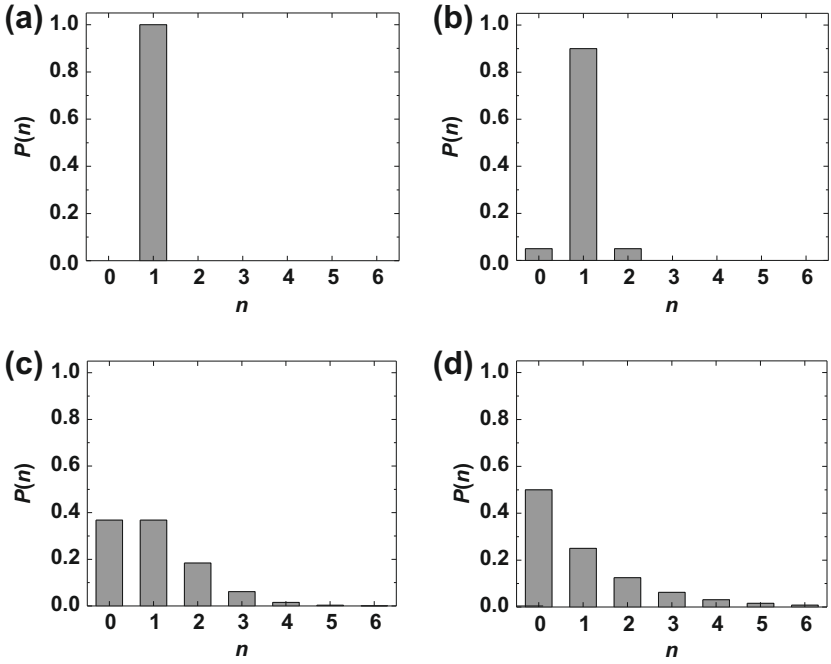

FIGURE 2.9 Photon number probability distributions of four pulsed sources, each with a mean photon number $\mu = 1$. (a) Ideal single-photon source, $g^{(2)}[0] = 0$. (b) Non-ideal single-photon source, $g^{(2)}[0] = 0.1$. (c) Coherent source, $g^{(2)}[0] = 1$. (d) Thermal source, $g^{(2)}[0] = 2$.

The photon statistics for a pulsed coherent source follow a Poisson probability distribution

$$P(n) = \frac{e^{-\mu}\mu^n}{n!}, \tag{2.88}$$

where $\mu = |\alpha|^2$ is the mean photon number per pulse. This distribution is shown in Fig. 2.9c for $\mu = 1$ and in Fig. 2.10c for $\mu = 0.1$. The second-order coherence of a coherent state is $g^{(2)}(\tau) = 1$ for all τ, as shown in Fig. 2.11c for a pulsed coherent source. Higher orders of coherence are also equal to unity: $g^{(m)}(\vec{\tau}) = 1$ for all $\vec{\tau}$. A stable single-mode laser operated well above threshold typically emits light that is a good approximation to a coherent state [25,15].

The photon probability distribution of a coherent state remains Poissonian after attenuation. Nonetheless, by attenuating a coherent state it is possible to make the two:one photon ratio

$$\frac{P(2)}{P(1)} = \frac{\mu}{2} \tag{2.89}$$

arbitrarily small; however, this improvement comes at the expense of a lowered mean photon number, μ, and hence a lowered source efficiency. As discussed in Sections 2.2.2 and 2.2.9, attenuation does not change the second-order coherence.

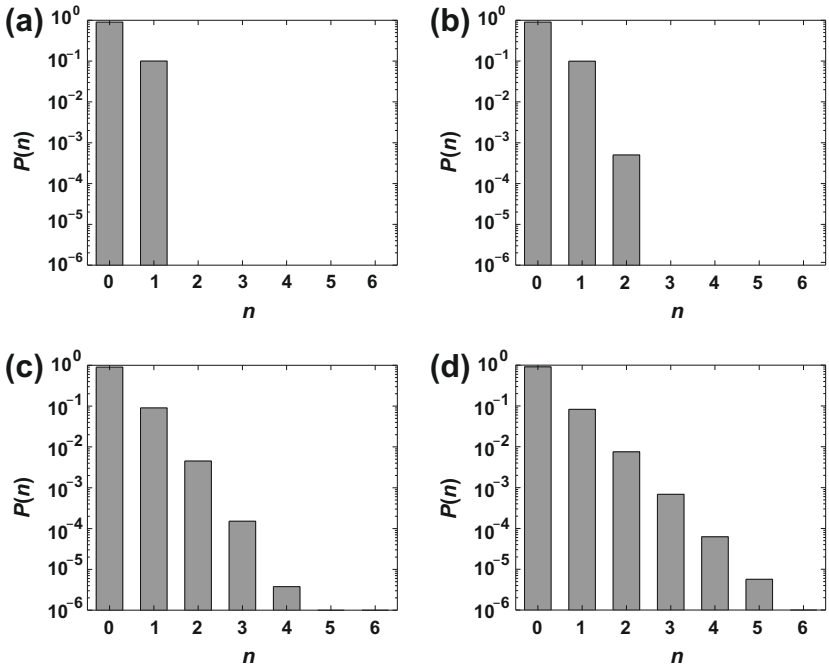

FIGURE 2.10 Photon number probability distributions of four pulsed sources with mean photon number $\mu = 0.1$. (a) Single-photon source with $g^{(2)}[0] = 0$. (b) Non-ideal single-photon source with $g^{(2)}[0] = 0.1$. (c) Coherent source, $g^{(2)}[0] = 1$. (d) Thermal source, $g^{(2)}[0] = 2$. Note the log scale on the $P(n)$ axis.

2.2.13.2 Thermal Source

The density matrix for a thermal source can be written [25]

$$\hat{\rho} = \sum_n \frac{\mu^n}{(1+\mu)^{n+1}} |n\rangle\langle n|. \tag{2.90}$$

This source has a photon probability distribution

$$P(n) = \frac{\mu^n}{(1+\mu)^{n+1}}. \tag{2.91}$$

The zero-delay values of the temporal coherences are $g^{(2)}(0) = 2$ and $g^{(m)}(\vec{0}) = m!$. Thus a thermal source is both *bunched*, since the zero-delay values of the coherences are higher than the values at non-zero delays, and *super-Poissonian*, since those values are greater than one.

In practice, a true thermal source is difficult to implement and characterize experimentally because coherence times of thermal sources are typically much shorter than the temporal resolution of single-photon detectors. As a substitute, one can make a pseudo-thermal source by scattering a CW laser off a time-dependent scattering medium, such as a rotating wheel of ground glass [2]. The

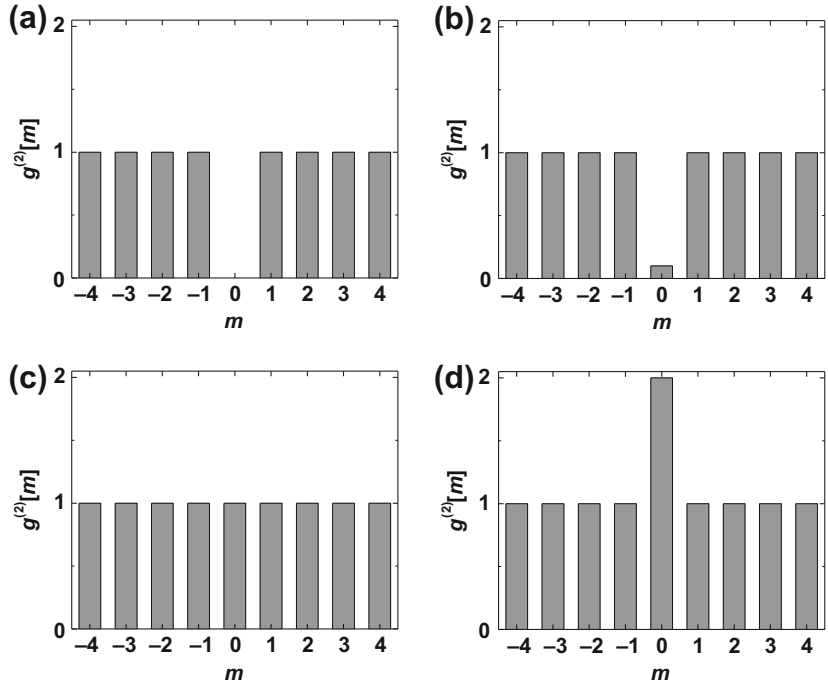

FIGURE 2.11 Second-order coherences of the four pulsed sources in Figs. 2.9 and 2.10: (a) single-photon source with $g^{(2)}[0] = 0$, (b) non-ideal single-photon source with $g^{(2)}[0] = 0.1$, (c) coherent source, and (d) thermal source. The height of each bar represents the total area of each pulse in the normalized correlation histogram.

resulting time-dependent speckle pattern is then sampled in the far field over an area small compared to the mean speckle size. The effective coherence time of the source can then be modified by adjusting the speed at which the scattering medium changes, for example, by adjusting the rotation speed of the ground glass wheel.

A thermal or pseudo-thermal source is sometimes referred to as a chaotic source, although it is chaotic only in the sense that it appears random, and has nothing to do with chaos theory. The bunching exhibited by a thermal source can be fully explained as intensity fluctuations of a classical electromagnetic field [25].

2.2.13.3 Pair Source

Photon pairs can be generated in many different ways. Common examples include atomic cascades (see Chapter 11), parametric downconversion (Chapter 12), and four-wave mixing (Chapter 13). The specifics of photon number distributions and coherences will depend on the details of the source, and are detailed for each type of source in subsequent chapters. Here, we focus

on one example, a two-mode squeezed state, which is the model state for photon pairs generated via parametric downconversion [16]:

$$|\xi_2\rangle = \exp\left(\xi^* \hat{a}_s \hat{a}_i - \xi \hat{a}_s^\dagger \hat{a}_i^\dagger\right)|0\rangle_s|0\rangle_i, \tag{2.92}$$

where $\xi = re^{i\theta}$ is the squeezing parameter and $\hat{a}_s^\dagger$ and $\hat{a}_i^\dagger$ denote creation operators acting on the signal and idler modes, respectively. For each photon created in the signal mode, a corresponding paired photon is created in the idler mode:

$$|\xi_2\rangle = \frac{1}{\cosh r} \sum_{n=0}^{\infty} e^{in\theta} (-\tanh\ r)^n |n\rangle_s |n\rangle_i. \tag{2.93}$$

The photon number probabilities for signal and idler are identical, $P_s(n) = P_i(n) = P(n)$, and can be written in terms of the mean photon number $\mu_s = \mu_i = \mu$ as

$$P(n) = \frac{(\tanh\ r)^{2n}}{(\cosh\ r)^2} = \frac{\mu^n}{(1+\mu)^{n+1}}. \tag{2.94}$$

Thus the number of photons in each follows a thermal distribution, with μ the average number of pairs generated.

One important application of a pair source is a heralded single-photon source, where detection of one member of the pair (idler) is used to herald the presence of the other (signal). Conditioning on detection of an idler photon decreases the probability of finding no photons in the signal field. This increases the effective (conditional) mean photon number $\mu_{\text{effective}}$ without significantly changing the two:one photon ratio $P(2)/P(1)$; as a result the ratio $2P(2)/[P(1)]^2$ decreases and $g^{(2)}[0]$ can drop below unity (see Eq. (2.50)). This can be seen by comparing Fig. 2.12a and b. If the mean pair number μ is lowered, this conditional $g^{(2)}[0]$ can be made arbitrarily close to zero. If there is loss in the heralding arm, the overall rate of heralded photons will drop, increasing the conditional $g^{(2)}[0]$ compared to lossless heralding detection, as illustrated in Fig. 2.12c. Channel losses in the heralded arm will cause a drop of only the overall rate of photons, but will not affect multi-photon suppression or $g^{(2)}[0]$ (see Fig. 2.12d). Practical issues related to heralded sources will be covered in greater detail in Chapters 11–13.

Taking into account the spectral composition of the signal and idler, and taking the low-squeezing limit, Eq. (2.92) can be approximated as [28]

$$|\xi_2\rangle \simeq \sqrt{1-\xi}|0\rangle_{\rm s}|0\rangle_{\rm i} + \sqrt{\xi}\int {\rm d}\omega_{\rm s} \int {\rm d}\omega_{\rm i} \Psi(\omega_{\rm s},\omega_{\rm i}) \hat{a}_{\rm s}^\dagger(\omega_{\rm s}) \hat{a}_{\rm i}^\dagger(\omega_{\rm i})|0\rangle_{\rm s}|0\rangle_{\rm i}, \tag{2.95}$$

where $\Psi(\omega_{\rm s},\omega_{\rm i})$ is the signal-idler joint wavefunction, which describes the amplitude distribution for creating a photon pair with signal frequency $\omega_{\rm s}$ and idler frequency $\omega_{\rm i}$. This joint wavefunction is determined by both energy conservation and phase-matching conditions, and can be characterized by measuring the joint spectral density. This will be discussed in Chapter 12.

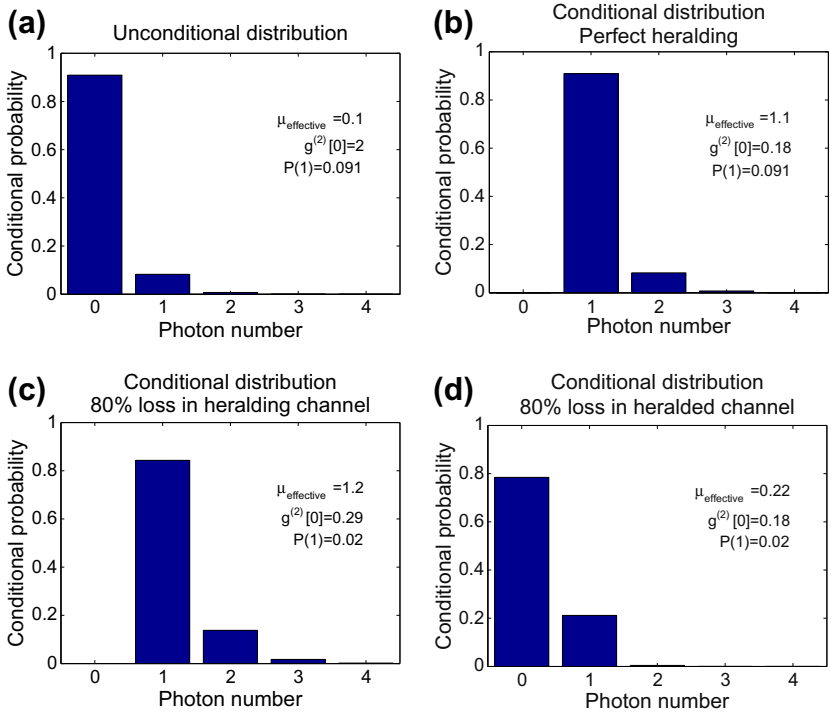

FIGURE 2.12 Basic principles of a heralded single-photon source based on a pair source, assuming a click/no-click single-photon detector (see Section 2.3.3.1) in the heralding arm. (a) Unconditional photon number distribution in each arm. Conditional photon number distribution of the heralded arm with (b) lossless heralding; (c) loss in heralding channel only; (d) loss in heralded channel only. $\mu_{\text{effective}}$ is the mean photon number in the heralded arm after conditioning on the heralding field and $P(1)$ is the overall, unconditional probability of producing one photon in the heralded arm. *Image courtesy of Elizabeth Goldschmidt.*

2.3 DETECTOR PROPERTIES

In its simplest, ideal form, a single-photon detector is a device that produces one electrical output pulse in response to a single input photon. The perfect detector would have a detection efficiency of 100 % and ideally would be able to resolve photon number. Timing latency, timing jitter, and dead time would all be zero. The ideal device would have no dark counts and zero probability of afterpulsing.

Not surprisingly, no existing detector satisfies all these criteria, and no one type of detector outperforms all others in all these metrics. For a given application, the choice of detector will typically involve trade-offs, where some of these characteristics are improved at the expense of others. This section will formally define the properties used to evaluate the performance of the detectors discussed in this book.

The single-photon detectors covered in this book can in general be categorized as photon counters. They give information only about the terms on the diagonal of the density matrix, when the density matrix is written in the photon-number-state basis. Photon-counting measurements, including $g^{(2)}$ measurements performed with photon-counting detectors, typically are sensitive only to certain characteristics of the modes of the photons under study. For example, photon-counting experiments are not typically sensitive to the details of the spatial, spectral and temporal mode profiles, except in the sense that detectors only count photons in the modes that reach the detectors, at wavelengths the detectors are sensitive to, and at times when the detectors are active. Hong-Ou-Mandel interference is a notable exception to this, as it is highly sensitive to overlap of the spatial, spectral, temporal, and polarization modes of the two incident photons. Other measurements, such as those of high-order coherences $g^{(n)}$, can yield information about the number and nature of multiple modes having different photon statistics [18].

Several other methods exist for measuring signals at the single-photon level, many of which involve mixing the single-photon field with a strong optical field and using a conventional (as opposed to single-photon) optical detector. These methods, which include homodyne tomography [29,36], heterodyne detection, and spectral interferometry [10], can yield information about the off-diagonal elements of $\hat{\rho}$. These techniques tend to be exquisitely sensitive to the mode, since they give information about only the modes of an optical state that overlap with the separately prepared strong optical field, which is often referred to as the local oscillator. These techniques are outside the scope of this book.

2.3.1 Detection Efficiency

One of the most important characteristics of a single-photon detector is its detection efficiency, η_{DE}. For a free-space coupled detector, η_{DE} represents the probability that a photon incident on the active area of the detector results in an electrical output of sufficient magnitude to be registered by the external electronics, provided that the detector and its electronics are armed and ready to sense an incoming photon. It should be noted that a detector often appears as a single package, which may have components required for its operation, such as a window on a hermetic package, or more sophisticated optics to guide light onto the active area of the detector. Because these components are inseparable parts of the device, their overall transmittance should be included in η_{DE}.

In a fiber-coupled detection system, the term detection efficiency can be somewhat more problematic to define because one must decide where the source to be measured ends and the detector begins. The preferred dividing line is within the portion of the detector's input fiber that is accessible for a connector or fusion splicing. Thus η_{DE} represents the fraction of photons that have been coupled into (or generated in) the optical fiber that yield a measurable electrical output, and is sometimes referred to as the "system detection efficiency" to

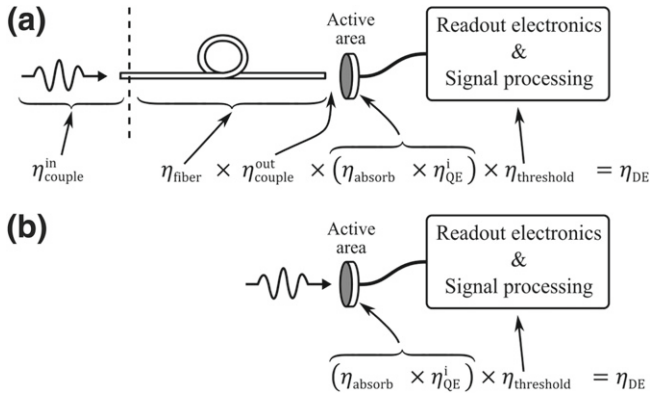

FIGURE 2.13 Illustration of decomposition of detection efficiency for (a) fiber-coupled and (b) free-space-coupled single-photon detector systems, where the dashed line indicates the demarcation between efficiencies associated with the detector and those associated with the experiment.

distinguish it from the detection efficiency of the bare detector. While this definition does not include the (invariably non-unity) efficiency of coupling from a free-space optical experiment into fiber, it does include losses within the fiber and losses associated with coupling light out of the fiber and onto the active area of the actual sensor. Thus it is important to remember that when using a fiber-coupled detector in a free-space experiment, η_{DE} must be reduced by the fiber input coupling efficiency to find the detection efficiency for that situation (see Fig. 2.13).

For a fiber-coupled detector, the system detection efficiency, η_{DE}, can be decomposed into a product of several discrete efficiencies [33]:

$$\eta_{DE} = \eta_{fiber}\eta^{out}_{couple}\eta_{absorb}\eta^{i}_{QE}\eta_{threshold}. \tag{2.96}$$

The first two component efficiencies quantify the efficiency with which light reaches the sensitive region of the detector. The fiber transmission, η_{fiber}, is typically quite high for visible and near-infrared wavelengths, unless particularly long fiber is used. The output coupling efficiency, η^{out}_{couple}, is a measure of the spatial overlap of the optical mode exiting the fiber with the active area of the detector. η^{out}_{couple} accounts for any misalignment or size mismatch between the output mode of the optical fiber and the active area of the device.

The third and fourth component efficiencies are intrinsic to the detector element itself. The absorption efficiency, η_{absorb}, is the fraction of photons incident on the detector active area that are absorbed. The internal quantum efficiency, η^{i}_{QE}, is the fraction of absorbed photons that yield an output electrical signal. When a fiber-coupled detector is used with a free-space experiment, remember to include η^{in}_{couple}, the coupling efficiency of the input light into the fiber, as a prefactor.

The threshold efficiency, $\eta_{threshold}$, quantifies the efficiency with which the output electrical signal is registered by external counting or timing electronics.

While $\eta_{\text{threshold}}$ is often unity or very close to it, this may not always be the case. For example, if electrical pulses resulting from dark counts (or background counts arising from detected background blackbody radiation) have a comparable but somewhat smaller amplitude than signal pulses, then a threshold in the external electronics may be adjusted to reduce the background count rate. In some cases, a trade-off can be made between $\eta_{\text{threshold}}$—and hence detection efficiency—and this background count rate [32,14].

For a free-space-coupled detector, the detection efficiency is the probability that a photon incident on the detector is recorded by the measurement electronics. In this case, the decomposition simplifies to

$$\eta_{\text{DE}} = \eta_{\text{absorb}} \eta_{\text{QE}}^{\text{i}} \eta_{\text{threshold}}. \tag{2.97}$$

There may be special cases for a free-space-coupled detector where the optical coupling system has a significant impact on the detector performance, for example if the detector's active area is especially small. In such a case, as for the fiber-coupled detector case, a coupling efficiency term, η_{couple}, should also be included in η_{DE}.

2.3.2 POVM Elements

The set of POVM (Positive-Operator-Valued-Measure) operators are useful for characterizing the outcome of measurements with a single-photon detector or detection system. The probability of obtaining result m, given an optical field described by the density matrix $\hat{\rho}$ and a detector with detection efficiency η_{DE} can be written as [37]

$$p_{\text{DE}}(m) = \text{Tr}\{\hat{\rho}\hat{\pi}_m\}, \tag{2.98}$$

where $\hat{\pi}_m$ is the detector POVM operator for outcome m and depends on η_{DE}.

The POVM operators of a detector that is only sensitive to the number of photons in an optical field (*i.e.*, the diagonal elements of $\hat{\rho}$ in the number state basis) can be written as

$$\hat{\pi}_m = \sum_{n=m}^{\infty} p(m|n)|n\rangle\langle n|, \tag{2.99}$$

where $p(m|n)$ is the conditional probability that detector records m photons at the output, given n photons at the input. In this case, we can write [9]

$$p_{\text{DE}}(m) = \sum_{n=m}^{\infty} p(m|n)P(n). \tag{2.100}$$

The form of the $\hat{\pi}_m$ matrices are given in the following section for two ideal detector types. In a real measurement system, the POVM elements will only approximate these ideal cases. Nonetheless, the $\hat{\pi}_m$ for each outcome m can be determined by performing detector tomography, as discussed in Chapter 9.

2.3.3 Photon-Number-Resolving (PNR) Capability

Single-photon detectors can be broadly grouped into three categories of PNR capability: "no," "some" or "full" PNR capability [7]. While these categories are of course somewhat arbitrary, they capture some essence of the fundamental operation of each type of device.

PNR capability can be useful in multiple distinct ways. For single-shot measurements, if the detector is to correctly identify the number of incident photons it is essential that η_{DE} be very close to 100%. For averaged or ensemble measurements, high detection efficiency is less critical: if one can determine the detector POVM elements with low uncertainty, then it should be possible to invert these POVM elements and recover the photon statistics of the incident light with high accuracy. Of course, this procedure works best with high detection efficiency.

2.3.3.1 No PNR Capability ("click/no-click" Detectors)

These are detectors that operate (or typically operate) as a one-or-more-photon or no-photon device. That is, they register only *whether* photons were detected, but do not provide information on the number of detected photons. These are variously referred to as "threshold," "click" or "click/no-click" detectors, and are the most readily available and widely used type of single-photon detectors. Examples discussed in this book include photomultiplier tubes (PMTs) in Chapter 3, single-photon avalanche diodes (SPADs) in Chapter 4, and superconducting nanowire single-photon detectors (SNSPDs) in Chapter 6.

For an ideal threshold detector, with no dark counts or afterpulsing and with detection efficiency η_{DE}, the POVM for no output is [22]:

$$\hat{\pi}_0 = \sum_{n=0}^{\infty} (1-\eta_{\mathrm{DE}})^{\mathrm{n}} |n\rangle\langle n|. \tag{2.101}$$

The probability of the detector delivering no output for this detection efficiency, $p_{\mathrm{DE}}(0)$, can be expressed in terms of the photon number probabilities of the incident light, $P(n)$, as

$$p_{\mathrm{DE}}(0) = \sum_{n=0}^{\infty} (1-\eta_{\mathrm{DE}})^{\mathrm{n}} P(n). \tag{2.102}$$

For this detector, the POVM for yielding a click is [21,22]

$$\hat{\pi}_{\mathrm{click}} = \sum_{n=1}^{\infty} [1-(1-\eta_{\mathrm{DE}})^{\mathrm{n}}] |n\rangle\langle n|. \tag{2.103}$$

Thus the probability of a click at the output is

$$p_{\mathrm{DE}}(\mathrm{click}) = \sum_{n=1}^{\infty} [1-(1-\eta_{\mathrm{DE}})^{\mathrm{n}}] P(n). \tag{2.104}$$

2.3.3.2 Some PNR Capability (Number Resolving Through Multiplexing)

This category consists of devices that are constructed by multiplexing individual non-PNR detectors. The maximum number of photons that these devices can resolve is obviously limited by the number of individual detectors and/or multiplexing pathways. Characteristics of the device can change with the number of photons detected and the spatial distribution of the illumination, since some of the individual elements or areas become unresponsive after firing. Crosstalk between individual elements may also degrade these characteristics, so any crosstalk—or evidence for lack thereof—should be discussed. Time-multiplexed systems will necessarily operate with an increased dead time compared to the individual elements, thus limiting the overall repetition rate.

Despite the potential downsides, these detectors can be quite useful provided the crosstalk is minimal and the number of individual elements or pathways is large compared to the number of incident photons. In fact, some detectors in this category outperform many detectors considered to have full PNR capability, most notably because some detectors in this latter category have very low system detection efficiencies.

Examples of detectors classified as having some PNR capability include the multi-element SNSPDs discussed in Chapter 6 and the time-multiplexed and space-multiplexed detection schemes described in Chapter 7. The visible light photon counter (VLPC) covered in Chapter 5 is a somewhat unusual example in this category, since it does not consist of individual, discrete detection elements; nonetheless, we include it in this category because a region of the detector is effectively "dead" (or "blocked") after detection of one photon leads to a controlled avalanche in that region.

2.3.3.3 Full (or Intrinsic) PNR Capability

Detectors with full PNR capability are devices whose output is inherently proportional to the number of photons, excluding usual saturation limits to which all detectors are subject. It has been suggested that a detector with full PNR capability is a device whose probability of detecting n photons scales *only* as η_{DE} without any other n-dependence. Detectors satisfying this definition of full PNR capability include the solid-state photomultiplier (SSPM) and quantum dot optically gated field effect transistor (QDOGFET), which are discussed in Chapter 5, and the transition edge sensor (TES) described in Chapter 6.

In the absence of dark counts and afterpulsing, the POVM describing how an ideal photon number-resolving detector gives an output indicating m detected photons is [22,41]

$$\hat{\pi}_m = \sum_{n=m}^{\infty} \binom{n}{m} \eta_{\mathrm{DE}}^m (1-\eta_{\mathrm{DE}})^{n-m} |n\rangle\langle n|. \tag{2.105}$$

Thus, the probability of this PNR detector registering m photons, for a detection efficiency of η_{DE}, can be computed from the photon number probabilities $P(n)$ as

$$p_{\mathrm{DE}}(m) = \sum_{n=m}^{\infty} \binom{n}{m} \eta_{\mathrm{DE}}^{m} (1-\eta_{\mathrm{DE}})^{n-m} P(n). \tag{2.106}$$

The conditional probability that the detector records m photons at the output, given exactly n photons at the input, is

$$p(m|n) = \binom{n}{m} \eta_{\mathrm{DE}}^{m} (1-\eta_{\mathrm{DE}})^{n-m}. \tag{2.107}$$

As an example, the probability of a PNR detector yielding a one-photon output is

$$p_{\mathrm{DE}}(1) = \sum_{n=1}^{\infty} n\eta_{\mathrm{DE}} (1-\eta_{\mathrm{DE}})^{n-1} P(n). \tag{2.108}$$

Expanding out the first few terms, we find

$$p_{\mathrm{DE}}(1) = \eta_{\mathrm{DE}}[P(1) + 2(1-\eta_{\mathrm{DE}})P(2) + 3(1-\eta_{\mathrm{DE}})^2 P(3) + \cdots] \tag{2.109}$$

If $\eta_{\mathrm{DE}} \simeq 1$, then $p_{\mathrm{DE}}(1)$ will tend to be dominated by the one-photon component of the input light. By contrast, if $\eta_{\mathrm{DE}} \ll 1$, higher photon number terms will play a more important role.

One way to characterize the number-resolving capability of a detector is to compute the fidelity of the measured $\hat{\pi}_m$ with the ideal $\hat{\pi}_m$ for each value of m, following the approach used by Feito *et al.* with classical input states sent to time-multiplexed detectors [9]. Brida *et al.* showed that this scheme can be improved by leveraging the nonclassical correlations of a parametric downconversion source [5].

An even more stringent test is to compute the fidelity with the ideal POVM elements for a PNR detector with $\eta_{\mathrm{DE}} = 1$; in this case, each ideal POVM element has a single component: $\hat{\pi}_m = \delta_{m,n}|n\rangle\langle n|$. A PNR detector having high fidelity with these POVM elements would be immensely powerful for single-shot measurements of photon number.

Another way to characterize PNR capability is to invert the measured POVM and find the fidelity of the reconstructed photon probability distributions with the incident $P(n)$'s.

In the situation considered so far in this section, outcomes m will only be incorrect because not all photons are detected ($\eta_{\mathrm{DE}} \neq 1$). In this case, $p(m|n)$ is zero for all $m > n$: one incident photon will never be misidentified as two photons, two will never be misidentified as three, and so on. Realistic PNR detectors can also misidentify the number of incident photons if there is significant variation in the amplitude of the output electrical pulses for a fixed number of incident photons. This variation is typically characterized by measuring a histogram of the distribution of pulse heights or areas, as is illustrated in the next section for the example of an energy-resolving detector.

2.3.3.4 Energy-Resolving Detectors

An energy-resolving detector is one whose output electrical pulse height (or area) is directly proportional to the energy of each absorbed photon. A notable example is the TES discussed in Chapter 6. The pulse-height distribution, when plotted with photon energy on the x-axis, can be used to determine the energy resolution, ΔE, which is the full-width-at-half-maximum (FWHM) of each peak in the distribution. For some detectors, the energy resolution depends on either the photon energy or the photon number; if so, $\Delta E(\hbar\omega)$ or $\Delta E(n)$ should be specified or plotted.

However, ΔE contains somewhat limited information about a detector's ability to resolve photon number. In many applications the most relevant quantity is the probability that detection events are associated with the wrong photon number. Unfortunately, it is typically not possible to independently measure the distributions for each individual photon number. Instead, a source such as an attenuated laser pulse with a Poisson distribution is typically used, and all the photon number peaks are measured at once. The overlap of adjacent peaks can be quantified by measuring the peak visibility, defined as [24]

$$V_{\text{peak}} = \frac{(max - min)}{(max + min)}, \tag{2.110}$$

where *max* is the average maximum value of two adjacent peaks and the *min* is the lowest value between these two maxima. V_{peak} may be determined from the raw histogram data or from more sophisticated multi-peak fitting routines [24].

Figure 2.14 illustrates simulated pulse-height distribution histograms for detectors with three different energy resolutions and two different photon energies. Each individual photon peak in this conceptual model has an ideal Gaussian shape—something that cannot necessarily be assumed about practical detectors [24]. In all four panels, the source is assumed to follow Poissonian statistics with mean photon number $\mu = 2$. Panels (a)–(c) illustrate the effect of changing the energy resolution for a fixed photon energy of $\hbar\omega = 1$ eV. The individual photon peaks are clearly well separated from one another in (a), where $\Delta E = 0.2\hbar\omega$ and $V_{\text{peak}} \simeq 1$ for all peaks. In (b), each peak overlaps just slightly with its neighboring peaks, yet only ~1% of detection events will misidentify the photon number. In this case, V_{peak} ranges from ~0.88 to ~0.90 for the peaks shown. In (c), the resolution is further degraded such that $\Delta E = \hbar\omega = 1$ eV, and peak visibility is undefined for all minima but one. In this case, a large fraction of photon numbers will be misidentified.

Figure 2.14d shows what happens when ΔE is held fixed at 1 eV (the same value as in Fig. 2.14c), but the photon energy is increased to 2.2 eV. The result looks much the same as in Fig. 2.14b. This illustrates another feature of energy-resolving detectors: in addition to resolving the number of photons at a fixed wavelength, they can also be used to distinguish single photons of different wavelengths, provided the photon energies are separated well enough to be resolved [6]. This can also present experimental challenges. For example, in a

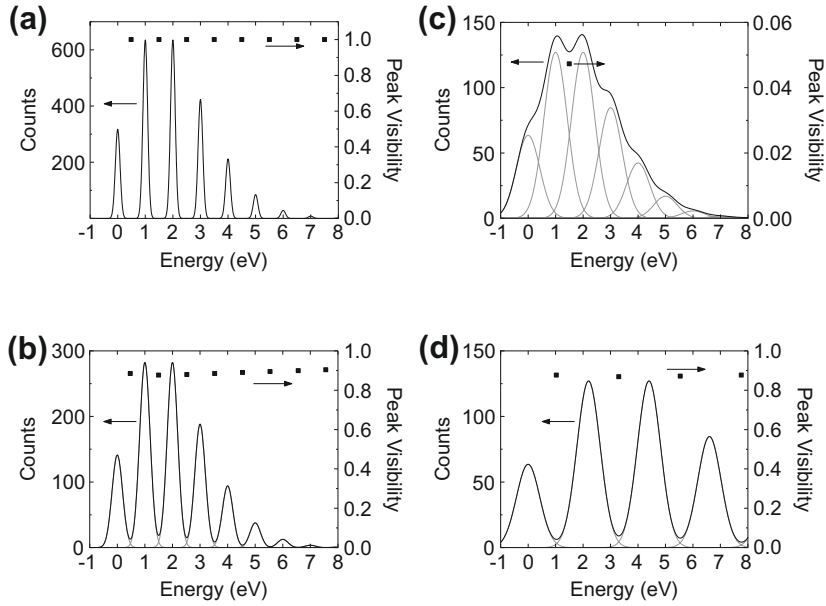

FIGURE 2.14 Simulated pulse energy distributions for an ideal energy-resolving detector, assuming Gaussian distributions for each photon number peak. Gray lines are individual photon number peaks and black lines are the sum of all the individual peaks. (a)–(c) Simulated histograms for a photon energy $\hbar\omega = 1$ eV for three different energy resolutions: (a) $\Delta E = 0.2$ eV, (b) $\Delta E = 0.45$ eV, (c) $\Delta E = 1$ eV $= \hbar\omega$. (d) Simulation for $\Delta E = 1$ eV, which is the same energy resolution as in (c), but with a higher photon energy of $\hbar\omega = 2.2$ eV. In these simulations, ΔE does not depend on energy or photon number. Visibilities (dots) are derived using Eq. (2.110).

parametric downconversion experiment, a single pump photon of energy $2\hbar\omega$ can be misidentified as two downconverted photons of energy $\hbar\omega + \hbar\omega$.

As well resolved as the individual photon peaks are in Fig. 2.14a, a detector with such a histogram is only useful for resolving photon number in a single-shot measurement if the detection efficiency is quite high. By contrast, a detector with the pulse-height distribution in Fig. 2.14c with $\eta_{\mathrm{DE}} \simeq 1$ would in many respects outperform a detector with the distribution in Fig. 2.14a, even if the latter had a relatively high detection efficiency of $\eta_{\mathrm{DE}} = 0.76$. This point is illustrated in Tables 2.1 and 2.2, which display the probability of outcome m given n input photons, $p(m|n)$, for the first few values of m and n. Table 2.1 shows these the probabilities for $\Delta E = \hbar\omega$ and $\eta_{\mathrm{DE}} = 1$; Table 2.2 shows them for $\Delta E = 0.2\hbar\omega$ and $\eta_{\mathrm{DE}} = 0.76$.

Note that in both cases, the probability of correctly identifying one photon at the input as one photon at the output is $p(1|1) \simeq 0.76$. As the incident photon number increases, the high-efficiency detector maintains $p(n|n) \simeq 0.76$, whereas the detector with better energy resolution but lower efficiency quickly degrades: $p(2|2) \simeq 0.58$ and $p(3|3) \simeq 0.44$.

TABLE 2.1 Expected values of $p(m|n)$, which is the probability of detector outcome m, given that n photons are incident on a detector with full (but non-ideal) number resolving capability ($\Delta E \simeq \hbar\omega$) that has ideal detection efficiency η_{DE}. In Tables 2.1–2.3, all values are rounded to the nearest 0.01 and values < 0.01 are omitted for clarity

		n			
		0	**1**	**2**	**3**
	0	0.88	0.12		
m	**1**	0.12	0.76	0.12	
	2		0.12	0.76	0.12
	3			0.12	0.76

TABLE 2.2 Expected values of $p(m|n)$ for a near-ideal number resolving detector ($\Delta E \simeq 0.2\hbar\omega$) with non-ideal detection efficiency $\eta_{DE} = 0.76$. Such a detector would have a pulse energy distribution shown in Fig. 2.14a

		n			
		0	**1**	**2**	**3**
	0	1	0.24	0.06	0.01
m	**1**		0.76	0.36	0.13
	2			0.58	0.42
	3				0.44

As a third example, Table 2.3 shows $p(m|n)$ for a detector that combines the sub-optimal energy resolution of the detector in Table 2.1 ($\Delta E = \hbar\omega$) with the efficiency of the detector in Table 2.2 ($\eta_{DE} = 0.76$). The matrix for in Table 2.3 is simply the product of the two matrices in Tables 2.1 and 2.2.

It should be emphasized that these tables have been computed for the conceptual model described in the text, about which we have much more information than we could typically obtain for a realistic PNR detector—unless it had very well-resolved photon number peaks like those in Fig. 2.14a. In nearly all cases, there will be some finite overlap of adjacent photon number peaks, and conclusions about the probability of photon number misidentification can only be drawn by making assumptions about the shape of the peaks in the overlapping region.

Also note that multiplexed detectors that operate by taking a digital summation of the number of elements that detect a photon will typically

TABLE 2.3 Expected values of $p(m|n)$ for a non-ideal number resolving detector ($\Delta E = \hbar\omega$) with non-ideal detection efficiency $\eta_{DE} = 0.76$

		n			
		0	**1**	**2**	**3**
	0	0.88	0.30	0.10	0.03
m	**1**	0.12	0.61	0.35	0.15
	2		0.09	0.48	0.38
	3			0.07	0.38

not suffer from the problem of overlapping peaks, and thus a pulse-height distribution plot is not necessary.

2.3.4 Timing Latency and Rise Time

The timing latency of a detector, t_{latency}, is the time that elapses between when a photon is incident on a detector or detector system and when the subsequent output electrical pulse crosses a given threshold level, as shown in Fig. 2.15. The choice of the threshold level is based on a variety of factors specific to a given detector: timing resolution, tradeoffs between signal strength and electronic noise, and the ability to trigger subsequent timing electronics are some examples of considerations relevant to the choice of threshold. The rise time of the output pulse, τ_{rise}, is often characterized as the time required for the electrical output signal to rise from 10 % to 90 % of its maximum value.

2.3.5 Timing Jitter

Timing jitter is a measure of the pulse-to-pulse variation in t_{latency}, and is typically determined by characterizing the instrument response function (IRF) of a detector [3]. A typical measurement scheme is shown in Fig. 2.16. A very short optical pulse from a laser is split at a beamsplitter. One beamsplitter

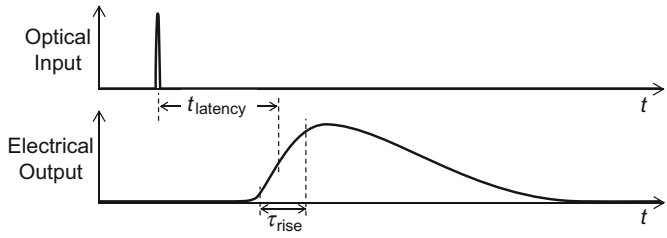

FIGURE 2.15 Illustration of definitions of timing latency, t_{latency}, and rise time, τ_{rise}.

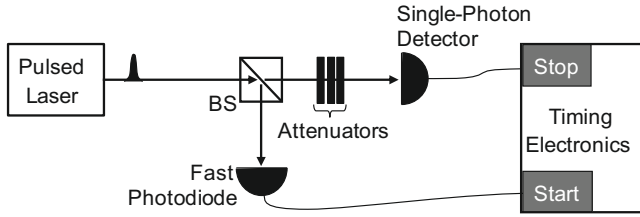

FIGURE 2.16 Typical setup for measuring a single-photon detector's instrument response function, which can be used to determine τ_{jitter}. The timing electronics here are operated in forward start-stop mode, where the fast photodiode (or alternatively the laser clock output, if available) starts a timer, and the signal from the single-photon detector stops the timer. For practical reasons, timing electronics are sometimes operated in reverse start-stop mode [3], where the single-photon detector starts the timer and the conventional fast photodiode stops it; this results in a time-reversed histogram, but will give the same value for τ_{jitter}.

output—comprised of a large, classical signal—is incident on a conventional fast photodiode. The other output of the beamsplitter is heavily attenuated before impinging on the single-photon detector. The timing electronics record a histogram of start-stop time delays that is proportional to the IRF.

The IRF measured using such a scheme will, in general, contain jitter contributions from several components, including the fast photodiode, the single-photon detector, and the timing electronics. The IRF may also be broadened due to the finite duration of the laser pulse. Ultrafast lasers with pulse durations < 1 ps and low-jitter (< 1 ps) conventional fast photodiodes are readily available; if these are used, the jitter is then largely dominated by contributions from the single-photon detector and the timing electronics, both of which are almost always greater than $\sim$20 ps FWHM, as discussed in Chapter 1. In some cases, it may be possible to deconvolve the various contributions to the IRF to estimate the jitter of the single-photon detector alone, but deconvolution should be performed with due care.

Figure 2.17 shows a measured IRF of a silicon SPAD, illustrating the definition of timing jitter, τ_{jitter}, which is the FWHM of the IRF. One can also specify $\tau_{\text{jitter}}^{(1\%)}$, which is the full-width at 1% of maximum of the IRF. For single-photon avalanche diodes, $\tau_{\text{jitter}}^{(1\%)}$ is often significantly larger that the FWHM, and is relevant when the signals of interest may arrive at a comparable time scale, such as in the case of quantum communications at GHz rates.

In some cases, the timing performance of a detector can depend on the detected count rate. In SPADs, for example, both jitter and latency have been shown to vary significantly for count rates above $\sim 1 \times 10^6$/s [39]. Pile-up may also affect a jitter measurement. Pile-up occurs when the timing electronics record only the first photon from an optical pulse, and are unable (during the recovery time of the detector and/or electronics) to record a second or third photon from that same pulse [3]. This will typically lead to an underestimate of the timing jitter. Careful measurement of jitter typically requires attenuating

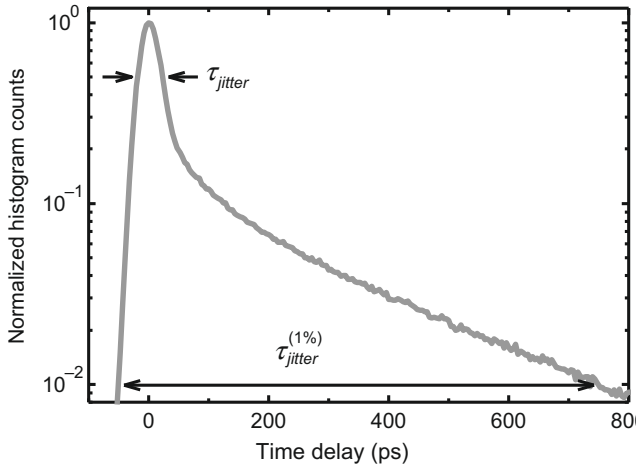

FIGURE 2.17 Example instrument response function illustrating the definitions of τ_{jitter} and $\tau_{\text{jitter}}^{(1\%)}$. For this device, τ_{jitter} is ~40 ps and $\tau_{\text{jitter}}^{(1\%)}$ is ~790 ps. *(Adapted from [43].)*

the optical pulse so that the count rate of the detector is much lower than the repetition rate of the laser. One can also test whether pile-up has affected a jitter measurement by observing whether τ_{jitter} is a function of the single-photon detection rate by decreasing the incident photon flux. Because of the potential for pile-up, and because it is important to know the effective timing jitter in a given measurement, the count rate and pump repetition rate (or the fraction of pump pulses in which a photon is detected), should accompany reported jitter measurements.

The timing jitter of detectors with partial or full number resolving capability may depend on the number of photons detected, so timing jitter may be specified separately for 1-photon events, 2-photon events, and so on.

2.3.6 Dead Time, Reset Time, and Recovery Time

The dead time, t_{dead}, is the duration of time, beginning at the start of a detection event, during which a detection system is incapable of producing an output electrical signal in response to additional incident photons. During the dead time, the detection efficiency is zero, as illustrated in Fig. 2.18. The dead time may be caused by intrinsic processes in the photosensitive system or it may be induced by external control systems in order to produce a particular performance characteristic.

The reset time, t_{reset}, is the time over which the detection efficiency increases from zero back to its initial value. If the detection efficiency approaches this initial value very slowly, it may be necessary to specify t_{reset} as the elapsed time after which the detection efficiency changes by less than some small percentage of its value.

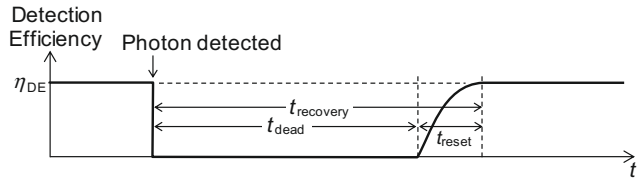

FIGURE 2.18 Example of detection efficiency plotted as a function of time. If the efficiency drops to zero after a photon is detected, then the dead time, t_{dead}, is the elapsed time until the efficiency is non-zero again. The reset time, t_{reset}, is the time required for the detection efficiency to recover to its initial value, η_{DE}. The recovery time, $t_{recovery}$, is the sum of t_{dead} and t_{reset}.

The total time required for the detection efficiency to recover to its steady-state value after a detection event is the recovery time, $t_{recovery} = t_{dead} + t_{reset}$. In detectors or systems with a very short reset time, $t_{dead} \simeq t_{recovery}$, and the terms can be used interchangeably.

The operation of the detector during its reset requires some special consideration. The fact that the detection efficiency is in transition during its reset can strongly affect measurements at high count rates. In addition, the reset action in some types of detectors (notably SPADs) can affect the ability of the electronics to sense a detection event that may have occurred during the reset. This is the origin of the so-called twilight events in some actively quenched SPAD detectors, and is discussed in Chapter 8.

2.3.7 Dark Count Rate

The dark count rate, R_{dark}, is the average number of counts registered by a detector per second when all input light to the detector is blocked.

2.3.8 Background Count Rate

In situations where not all background photons can be adequately blocked from reaching a detector, the background count rate, $R_{backgound}$, is sometimes quoted. While $R_{backgound}$ is not an intrinsic property of a detector, some detectors are more susceptible to it than others, especially those that are sensitive to mid- or far-infrared photons present in room-temperature blackbody radiation.

2.3.9 Afterpulse Probability

The afterpulse probability, $P_{afterpulse}$, is the excess probability for a detector to output an additional dark count due to a preceding detection event. The time interval over which the dark count probability is elevated should also be specified. Because $P_{afterpulse}$ can depend on the overall count rate, the afterpulse rate at the zero-count-rate limit should be distinguished from the afterpulse probability at higher count rates. In cases where the afterpulsing probability is

especially high, it may be reduced by gating the detector. Afterpulsing is most commonly observed in SPADs.

2.3.10 Active Area

The active area of a detector, A_{active}, is the area of the absorbing region of the device, assuming normal incidence. It is typically fairly easy to couple all of the incident light to a device with $A_{\text{active}} > 100 \times 100\ \mu\text{m}^2$. By contrast, for devices with active areas $10 \times 10\ \mu m^2$ of or less, η_{couple} may be compromised and may have to be included in the definition of η_{DE}.

2.3.11 Operating Temperature of Active Area

The operating temperature of a detector can present obstacles to implementation. For example, superconducting detectors can exhibit many outstanding characteristics, but must operate in cryogenic systems. As a result, light must typically be coupled to the devices through an optical fiber.

ACKNOWLEDGMENTS

The author is indebted to J. Bienfang, B. Calkins, J. Fan, M. Förtsch, T. Gerrits, S. Glancy, E. Goldschmidt, A. Lamas-Linares, F. Marsili, A. Migdall, R. Mirin, S. Nam, S. Polyakov, K. Shalm, K. Silverman and N. Tomlin for many helpful conversations and comments on the chapter.

REFERENCES

[1] M. Aßmann, F. Veit, M. Bayer, C. Gies, F. Jahnke, S. Reitzenstein, S.Höfling, L. Worschech, and A. Forchel, "Ultrafast Tracking of Second-Order Photon Correlations in the Emission of Quantum-Dot Microresonator Lasers," Phys. Rev. B 81, 165314 (2010).
[2] F.T. Arecchi, "Measurement of the Statistical Distribution of Gaussian and Laser Sources," Phys. Rev. Lett. 15, 912 (1965).
[3] W. Becker, Advanced Time-Correlated Single Photon Counting Techniques, Vol. 81 (2005) (Springer Series in Chemical Physics).
[4] A. Beveratos, S.Kühn, R. Brouri, T. Gacoin, J.-P. Poizat, and P. Grangier, "Room Temperature Stable Single-Photon Source," Eur. Phys. J. D 18, 191–196 (2002).
[5] G. Brida, L. Ciavarella, I.P. Degiovanni, M. Genovese, A. Migdall, M.G. Mingolla, M.G.A. Paris, F. Piacentini, and S.V. Polyakov, "Ancilla-Assisted Calibration of a Measuring Apparatus," Phys. Rev. Lett. 108, 253601 (2012).
[6] B. Cabrera, R.M. Clarke, P. Colling, A.J. Miller, S. Nam, and R.W. Romani, "Detection of Single Infrared, Optical, and Ultraviolet Photons Using Superconducting Transition Edge Sensors," Appl. Phys. Lett. 73, 735 (1998).
[7] M.D. Eisaman, J. Fan, A. Migdall, and S.V. Polyakov, "Invited Review Article: Single-Photon Sources and Detectors," Rev. Sci. Instrum. 82, 071101 (2011).
[8] S. Fasel, O. Alibart, S. Tanzilli, P. Baldi, A. Beveratos, N. Gisin, and H. Zbinden, "High-Quality Asynchronous Heralded Single-Photon Source at Telecom Wavelength," New J. Phys. 6, 163 (2004).
[9] A. Feito, J.S. Lundeen, H. Coldenstrodt-Ronge, J. Eisert, M.B. Plenio, and I.A Walmsley, "Measuring Measurement: Theory and Practice," New J. Phys. 11, 093038 (2009).

[10] D.N. Fittinghoff, J.L. Bowie, J.N. Sweetser, R.T. Jennings, M.A. Krumbügel, K.W. DeLong, R. Trebino, and I.A. Walmsley, "Measurement of the Intensity and Phase of Ultraweak, Ultrashort Laser Pulses," Opt. Lett., 21, 884–886 (1996).
[11] E.B. Flagg, A. Muller, S.V. Polyakov, A. Ling, A. Migdall, and G.S. Solomon, "Interference of Single Photons from Two Separate Semiconductor Quantum Dots," Phys. Rev. Lett. 104, 137401 (2010).
[12] E.B. Flagg, S.V. Polyakov, T. Thomay, G.S. Solomon, "Dynamics of Nonclassical Light from a Single Solid-State Quantum Emitter," Phys. Rev. Lett. 109, 163601 (2012).
[13] A. M. Fox, Quantum optics: an introduction. Oxford University Press, Oxford, New York (2006).
[14] D. Fukuda, G. Fujii, T. Numata, K. Amemiya, A. Yoshizawa, H. Tsuchida, H. Fujino, H. Ishii, T. Itatani, S. Inoue, and T. Zama, IEEE Trans. Appl. Superdond. 21, 241–245 (2011).
[15] J.C. Garrison, and R.Y. Chiao, Quantum Optics. Oxford University Press, Oxford, New York (2008).
[16] C.C. Gerry and P.L. Knight, Introductory Quantum Optics. Cambridge University Press, New York (2005).
[17] R.J. Glauber, "Optical Coherence and Photon Statistics," in edited by C. deWitt, A. Blandin, and C. Cohen-Tannoudji, Quantum Optics and Electronics (Les Houches 1964), Gordon and Breach, New York, pp. 63–185 (1965).
[18] E.A. Goldschmidt, F. Piacentini, I.R. Berchera, S.V. Polyakov, S. Peters, S. Kück, G. Brida, I.P. Degiovanni, A. Migdall, M. Genovese, "Mode reconstruction of a light field by multi-photon statistics," Phys. Rev. A 88, 013822 (2013).
[19] R. Hanbury Brown and R.Q. Twiss, "Correlations between photons in two coherent beams of light," Nature 177, 27–29 (1956).
[20] C.K. Hong, Z.Y. Ou, and L. Mandel,"Measurement of subpicosecond time intervals between two photons by interference," Phys. Rev. Lett. 59 2044–2046, (1987).
[21] P. Kok and S.L. Braunstein, Phys. Rev. A 61, 042304 (2000).
[22] P. Kok, W.J. Munro, Kae Nemoto, T.C. Ralph, Jonathan P. Dowling, and G.J. Milburn, "Linear Optical Quantum Computing with Photonic Qubits," Rev. Modern Phys. 79, 135–174 (2007).
[23] J. Lee, M.S. Kim, and C. Brukner, Phys. Rev. Lett. 91, 087902 (2003).
[24] Z.H. Levine, T. Gerrits, A.L. Migdall, D.V. Samarov, B. Calkins, A.E. Lita, S.W. Nam, "Algorithm for Finding Clusters with a Known Distribution and its Application to Photon-Number Resolution Using a Superconducting Transition-Edge Sensor," J. Opt. Soc. Am. B 29, 2066 (2012).
[25] R. Loudon, The Quantum Theory of Light, 3rd Ed. Oxford University Press, Oxford, New York (2000).
[26] R. Loudon and P.L. Knight, J. Mod. Optics 34, 709–759 (1987).
[27] J.S. Lundeen, A. Feito, H. Coldenstrodt-Ronge1, K.L. Pregnell, Ch. Silberhorn, T.C. Ralph, J. Eisert, M.B. Plenio, and I.A. Walmsley, Tomography of quantum detectors. Nature Phys. 5, 27–30 (2009).
[28] A.I. Lvovsky, Wojciech Wasilewski, and Konrad Banaszek, "Decomposing a Pulsed Optical Parametric Amplifier into Independent Squeezers," Journal of Modern Optics 54, 721–733 (2007).
[29] A.I. Lvovsky and M.G. Raymer, Continuous-Variable Optical Quantum-State Tomography. Rev. Mod. Phys. 81, 299–332 (2009).
[30] L. Mandel, "Squeezed States and Sub-Poissonian Photon Statistics," Phys. Rev. Lett. 49, 136–138 (1982).
[31] A.J. Miller, S.W. Nam, J.M. Martinis, and A.V. Sergienko, Demonstration of a Low-Noise Near-Infrared Photon Counter with Multiphoton Discrimination. Appl. Phys. Lett. 83, 791–793 (2003).
[32] A.J. Miller *et al.* in Proc. of the 8th Int. Conf. Quantum Comm. Meas. Comp, 445 (2007).
[33] Aaron J. Miller, Adriana E. Lita, Brice Calkins, Igor Vayshenker, Steven M. Gruber, and Sae Woo Nam, "Compact Cryogenic Self-Aligning Fiber-to-Detector Coupling with Losses Below One Percent," Opt. Express 19, 9102–9210 (2011).
[34] P.J. Mosley, Generation of Heralded Single Photons in Pure Quantum States, Ph. D. Dissertation, University of Oxford (2007).
[35] P.J. Mosley, J.S. Lundeen, B.J. Smith, P. Wasylczyk, A.B. U'Ren, C. Silberhorn, and I.A. Walmsley, Phys. Rev. Lett. 100, 133601 (2008).

[36] C.R. Müller, B. Stoklasa, C. Peuntinger, C. Gabriel, J. Řeháček, Z. Hradil, A.B. Klimov, G. Leuchs, Ch. Marquardt, and L.L.Sánchez-Soto, "Quantum Polarization Tomography of Bright Squeezed Light," New J. Phys. 14, 085002 (2012).
[37] M.A. Nielsen and I.L. Chuang, Quantum Computation and Quantum Information. Cambridge University Press, Cambridge (2000).
[38] H. Qian and E.L. Elson, Fluorescence Correlation Spectroscopy with High-Order and Dual-Color Correlation to Probe Nonequilibrium Steady States," Proc. Natl. Acad. Sci. 101, 2828–2833 (2004).
[39] I. Rech, I. Labanca, M. Ghioni, S. Cova, "Modified Single Photon Counting Modules for Optimal Timing Performance," Rev. Sci. Instrum. 77, 033104 (2006).
[40] C. Santori, Generation of Nonclassical Light Using Semiconductor Quantum Dots, Ph.D. Dissertation, Stanford University (2003).
[41] M.O. Scully, and W.E. Lamb, Phys. Rev.179, 368 (1969).
[42] G.A. Steudle, S. Schietinger, D. Höckel, S.N. Dorenbos, I.E. Zadeh, V. Zwiller, O. Benson, "Measuring the Quantum Nature of Light with a Single Source and a Single Detector," Phys. Rev. A 86, 053814 (2012).
[43] M.J.Stevens, R.H. Hadfield, R.E. Schwall, S.W. Nam, R.P. Mirin, J.A. Gupta, "Fast lifetime measurements of infrared emitters using a low-jitter superconducting single-photon detector," Appl. Phys. Lett. 89, 031109 (2006).
[44] M.J. Stevens, S. Glancy, S.W. Nam, R.P. Mirin, "Third-Order Antibunching from an Imperfect Single-Photon Source," (2013) (To be submitted).
[45] E. Waks, C. Santori, Y. Yamamoto, "Security Aspects of Quantum Key Distribution with Sub-Poisson Light," Phys. Rev. A 66, 042315 (2002).
[46] E. Waks, E. Diamanti, B.C. Sanders, S.D. Bartlett, and Y. Yamamoto, "Direct Observation of Nonclassical Photon Statistics in Parametric Down-Conversion," Phys. Rev. Lett. 92, 113602 (2004).
[47] D.F. Walls, and G.J. Milburn, Quantum Optics, 2nd Ed., Heidelberg, Springer, Berlin (2008).
[48] X.T. Zou and L. Mandel, "Photon-antibunching and sub-Poissonian photon statistics," Phys. Rev. A 41, 475 (1990).
[49] H.-A. Bachor and T. C. Ralph, A Guide to Experiments in Quantum Optics, 2nd Edition, Wiley-VCH (2004).
[50] L. Mandel and E. Wolf, Optical Coherence and Quantum Optics, Cambridge University Press (1995).
[51] T. Gerrits, M.J. Stevens, B. Baek, B. Calkins, A. Lita, S. Glancy, E. Knill, S.W. Nam, R.P. Mirin, R.H. Hadfield, R.S. Bennink, W.P. Grice, S. Dorenbos, T. Zijlstra, T. Klapwijk, and V. Zwiller, "Generation of degenerate, factorizable, pulsed squeezed light at telecom wavelengths," Optics Exp. 19, 24434 (2011).